The autism-associated gene SYNGAP1 regulates human cortical neurogenesis

Marcella Birtele[1,2]#, Ashley Del Dosso[1,2]#, Tiantian Xu[1,2], Tuan Nguyen[1,2], Brent Wilkinson[3,4], Jean-Paul Urenda[1,2], Gavin Knight[5,6], Roger Moore[7], Ritin Sharma[7,8], Patrick Pirrotte[7,8], Randolph S. Ashton[5,6], Eric J. Huang[9,10], Marcelo P. Coba[3,4,11], Giorgia Quadrato[1,2*]

#Authors contributed equally

[1]Department of Stem Cell Biology and Regenerative Medicine, Keck School of Medicine, University of Southern California, Los Angeles, CA 90033, USA

[2]Eli and Edythe Broad CIRM Center for Regenerative Medicine and Stem Cell Research at USC, Keck School of Medicine, University of Southern California, Los Angeles, CA 90033, USA

[3]Department of Psychiatry and Behavioral Sciences, Keck School of Medicine, University of Southern California, Los Angeles, CA 90033, USA

[4]Zilkha Neurogenetic Institute, Keck School of Medicine, University of Southern California; Los Angeles, CA 90033, USA

[5]Department of Biomedical Engineering, University of Wisconsin-Madison, Madison, WI, 53706, USA

[6]Wisconsin Institute for Discovery, University of Wisconsin-Madison, Madison, WI, 53715, USA

[7]Integrated Mass Spectrometry Shared Resource, City of Hope Comprehensive Cancer Center, Duarte, CA, USA

[8]Cancer & Cell Biology Division, Translational Genomics Research Institute, Phoenix, AZ, USA

[9]Department of Pathology, University of California, San Francisco, CA 94143, USA

[10]Eli and Edythe Broad Institute for Stem Cell Research and Regeneration Medicine, University of California, San Francisco, CA 94143, USA

[11]Department of Physiology and Neuroscience, Keck School of Medicine, University of Southern California, 1501 San Pablo Street, Los Angeles, CA, 90033

* Correspondence should be addressed to: quadrato@usc.edu

Abstract

Autism spectrum disorder (ASD) is a genetically heterogeneous disorder linked with rare, inherited and *de novo* mutations occurring in two main functional gene categories: gene expression regulation and synaptic function[1]. Accumulating evidence points to dysregulation in cortical neurogenesis as a convergent mechanism in ASD pathophysiology[2-8]. While asynchronous development has been identified as a shared feature among ASD-risk genes in the category of gene expression regulation, it remains unknown whether this phenotype is also associated with ASD-risk genes in the synaptic function category. Here we show for the first time the expression of the synaptic Ras GTP-ase activating protein 1 (SYNGAP1), one of the top ASD risk genes[9], in human cortical progenitors (hCPs). Interestingly, we found that multiple components of the postsynaptic density (PSD) of excitatory synapses, of which SYNGAP1 is one of the most abundant components [10,11], are enriched in the proteome of hCPs. Specifically, we discover that SYNGAP1 is expressed within the apical domain of human radial glia cells (hRGCs) where it lines the wall of the developing cortical ventricular zone colocalizing with the tight junction-associated protein and MAGUK family member TJP1. In a cortical organoid model of SYNGAP1 haploinsufficiency, we show dysregulated cytoskeletal dynamics that impair the scaffolding and division plane of hRGCs, resulting in disrupted lamination of the cortical plate and accelerated maturation of cortical projection neurons. Overall, the dual function of SYNGAP1 in neuronal synapses and progenitor cells reframes our understanding of the pathophysiology of SYNGAP1-related disorders and, more broadly, underscores the importance of dissecting the role of synaptic genes associated with neurodevelopmental disorders in distinct cell types across developmental stages.

Introduction

Exome sequencing analyses have identified two major functional categories of genes associated with Autism Spectrum Disorder (ASD): gene expression regulation and synaptic function[1]. SYNGAP1 is a top ASD genetic risk factor [9] and one of the most abundant proteins found at the postsynaptic density (PSD) of excitatory synapses[10,11]. Within the PSD SYNGAP1 functions as a RAS GTPase-activating (RASGAP) protein that regulates synaptic plasticity [10-15]. Through its RASGAP domain, SYNGAP1 limits the activity of the mitogen-activated protein kinase 1 (Mapk1/Erk2), through its PDZ-binding domain, SYNGAP1 helps assemble the core scaffold machinery of the PSD[16-18]. Despite its classification as a synaptic protein, several lines of evidence suggest a potential role for SYNGAP1 at early stages of cortical neurogenesis. First, homozygous deletion of SYNGAP1 in embryonic mice leads to early developmental lethality [19]. Second, disruption of the SYNGAP1 signaling complex in embryonic mice results in deficits in the tangential migration of GABAergic interneurons [20]. Third, in addition to being an ASD genetic risk factor, *de novo* mutations in SYNGAP1 have been found in patients with intellectual disability, epilepsy, neurodevelopmental disability, and global developmental delay [21-23]. This evidence, combined with the high frequency and penetrance of pathogenic SYNGAP1 variants, indicates a major and unique role for SYNGAP1 in human brain development. However, as with other components of the scaffold machinery of the PSD, it remains unclear if SYNGAP1 is expressed in early cortical progenitors and how it affects cortical neurogenesis.

To address these questions, we used 3D cultures of human brain organoids. Derived from human embryonic or induced pluripotent stem cells (hPSCs), organoids have emerged as an effective way to model genetic architecture and cellular features of human brain development and disease [4,5,24-31]. These reproducible models of the human forebrain are capable of generating cellular diversity and epigenetic states that follow the developmental trajectory of the corresponding endogenous cell types [2,32-36], allowing for the functional characterization of ASD-risk genes in a longitudinal modeling and human cellular context.

Here, we show for the first time the expression of SYNGAP1 in human radial glia cells (hRGCs). Mechanistically, we find that SYNGAP1 regulates cytoskeletal remodeling of subcellular and intercellular components of hRGCs. In addition, we observe that this function is dependent on and

specific to the signaling pathways regulated by the RASGAP domain of SYNGAP1, with haploinsufficiency leading to disrupted organization of the developing cortical plate. By performing single-cell transcriptomics coupled with structural and functional analysis of mutant organoids, we discovered that SYNGAP1 regulates the timing of hRGCs differentiation with haploinsufficient organoids exhibiting accelerated maturation of cortical projection neurons. Altogether, these findings reveal a novel function for the classically defined synaptic protein SYNGAP1 at early stages of human cortical neurogenesis, providing a new framework for understanding ASD pathophysiology.

Results

SYNGAP1 is expressed in human ventricular radial glia and colocalizes with the tight junction protein TJP1.

SYNGAP1 expression has been reported to be largely restricted to the PSD of mature excitatory synapses[10,11] of mouse cortical projection neurons, where it has a cell type-specific function[37,38]. To investigate the expression of SYNGAP1 in distinct human cortical cell types, we took advantage of a recently published single cell RNA-seq data set of early human fetal telencephalic/cortical development from post-conception days (PCD) 26 to 54 [39]. We compared SYNGAP1 expression and distribution across all developmental stages with the expression of well-known gene markers for neuroepithelial/radial glial cells (PAX6), radial glial cells (HES5), and intermediate progenitor cells (IPC) (EOMES/TBR2) (Suppl. Fig 1a). Within the data set, SYNGAP1 expression was detected throughout the age range. Interestingly, SYNGAP1's expression levels were enriched in hRGCs (Suppl. Fig 1b,c), pointing to a novel function of SYNGAP1 in human cortical progenitors.

To further validate SYNGAP1 protein expression at this stage of development, we performed a proteome profiling of human cortical organoids (D.I.V. 7), which are entirely composed of Sox2+ and Pax6+ progenitors at this stage of development (Suppl. Fig. 1d). Using this pipeline, we were able to identify a total of 8691 proteins (Suppl. Table 1), including 24 unique peptides for SYNGAP1. Interestingly, 793 of these proteins belonged to the SynGO ontology term 'Synapse'(Suppl. Table 2), with enrichment in components of the postsynaptic density, pointing

to an unappreciated role of classically defined postsynaptic proteins in progenitor biology (Fig. 1a). Within 2-month-old organoids, the Ventricular Zone (VZ) is delineated by radially aligned Sox2+ neural stem cells surrounding the apical junctional belt, which is composed of adherens and tight junction proteins such as TJP1. Immunofluorescence revealed that SYNGAP1 expression was enriched at the apical endfeet side of the VZ cells (Fig. 1b) as well as in MAP2+ neurons (Fig.1d). Notably, SYNGAP1 and TJP1 co-localize (Fig. 1b). Through a series of immunohistochemical analyses of microdissected VZ and SVZ specimens of human cortex at gestational week 17 (GW17) (Fig. 1f) and mouse cortex at E13.5 (Suppl. Fig. 1e), we confirmed the same pattern of SYNGAP1 expression in the apical endfeet of ventricular radial glia cells. Moreover, SYNGAP1 immunoprecipitation and mass spectrometry analysis shows that TJP1 is part of the SYNGAP1 interactome (Fig. 1c, Suppl. Table 3). The PDZ ligand domain of SYNGAP1 is known to mediate localization of the protein to the PSD via binding to MAGUK proteins such as Dlg4 in mature neurons[40].TJP1 is a MAGUK that shares the modular-domain composition of other MAGUK family members, and therefore can associate to SYNGAP1 through a PDZ domain. Therefore, we hypothesize that SYNGAP1 interacts with TJP1, a PDZ domain containing protein, in a similar manner (Fig. 1e). The capacity of SYNGAP1 to associate to proteins containing PDZ domains is isoform-dependent[16,41]. To address whether hRGCs express the SYNGAP1 isoform alpha 1 (id: A0A2R8Y6T2), the isoform with the capacity to associate to PDZ domains, we designed a parallel reaction monitoring experiment based on high resolution and high precision mass spectrometry. This assay allowed us to show that similarly to what occurs in mature rodent synapses[16,41], SYNGAP1 has the capacity to associate to PDZ containing proteins in hRGCs cells (Fig. 1e, Suppl. Fig. 2a-b).

SYNGAP1's RASGAP domain is needed for cytoskeletal organization in hRGCs.

To uncover the unknown function of SYNGAP1 in human radial glia, we took advantage of an early cortical organoid model (D.I.V. 7) of SYNGAP1 haploinsufficiency. For this, we generated iPSC lines from a patient carrying a p.Q503X mutation in the RASGAP domain and from the corrected isogenic control (Suppl. Fig. 3b-e). We performed bulk RNA sequencing of 7 D.I.V. organoids from the SYNGAP1 p.Q503X and corrected lines, and our Gene Ontology (GO) analyses found terms for biological processes related to cytoskeletal remodeling and migration to

be significantly enriched within our gene list (P value = 1.02e-03) (Fig. 2a; Suppl. Table 4). In addition, GO analysis of the SYNGAP1 interactome revealed that the predicted set of molecular functions regulated by SYNGAP1 clustered within the functional categories of cytoskeletal organization and regulation (Suppl. Fig. 3a).

hRGCs have a bipolar shape with distinct apical and basolateral domains and include a process terminating at the ventricular surface and another process reaching the pial surface. To monitor the effect of SYNGAP1 haploinsufficiency on the shape and polarity of hRGCs processes, we employed a standardized single neural rosette protocol[42] that allows high-throughput generation and analysis of rosette formation (Fig. 2b,c,e; Suppl. Video 1). We found homogeneous expression of the cortical progenitor markers Pax6 and Sox2 with radially organized acetylated tubulin networks in rosettes derived from the SYNGAP1 p.Q503X corrected line (Fig. 2c,d). However, these structures were less organized in SYNGAP1 haploinsufficient tissues, and their formation was less frequent than in corrected rosettes (Fig. 2 e,f). Through a high throughput analysis of the localization tight-junction marker TJP1 in single rosettes tissues, we found that SYNGAP1 haploinsufficient rosettes exhibited apico-basal polarity from a wider, more irregular TJP1 positive region, while corrected individual rosettes had a tighter and more circular TJP1 ring (Fig. 2g-i, Suppl. Fig. 3f).

The ability of SYNGAP1 to partake in cytoskeletal remodeling in mature neurons has been attributed to enzymatic activity from its RAS GTPase-activating domain[10,11,38,43,44]. To assess if SYNGAP1's enzymatic function is conserved in hRGCs, we generated an iPSC line carrying a non-functional RASGAP domain (Suppl. Fig. 3g-i) and compared it to its isogenic control iPSC line. We observed a more marked effect compared to the SYNGAP1 haploinsufficient phenotype, with the tissue generated from the RASGAP-Dead (RGD) line displaying fully disrupted apico-basal polarity and a reduced central TJP1 positive luminal space (Fig. 2j-n; Suppl. Fig.3j). These data indicate both impairment in the cytoskeletal architecture of apical endfeet, as well as disruption of radial elongation of the basal process of hRGCs in both patient and RGD-derived tissues.

Next, we dissociated individual cells from rosettes derived from SYNGAP1 haploinsufficient early

cortical organoids, which displayed disrupted cytoskeletal organization. In the dissociated cells, we detected higher levels of f-actin with more disorganized filaments compared to the cells derived from the corrected organoids (Suppl. Fig. 3k-m). Similar characteristics were observed in cells derived from RGD and isogenic control organoids (Suppl. Fig. 3n-o).

To understand the contribution of the patient's genetic background to the observed phenotypes, we generated a line carrying the p.Q503X mutation in a control background (Suppl. Fig. 3p-r). Importantly, single rosettes generated from this line displayed the same phenotypes as SYNGAP1 p.Q503X (Suppl. Fig. 3s-t). This indicates that the SYNGAP1 haploinsufficiency phenotype is not influenced by the individual genomic context. This finding is consistent with the high penetrance of pathogenic SYNGAP1 variants in patients.

Altogether, these data show that SYNGAP1 regulates a dynamic cytoskeletal network that influences the subcellular and intercellular organization of ventricular radial glia. Furthermore, this function is dependent on and specific to the signaling pathways regulated by the RASGAP domain of SYNGAP1.

SYNGAP1 haploinsufficiency disrupts the organization of the developing cortical plate.

hRGCs control the generation and organization of a proper VZ by tightly connecting to each other via an AJ belt at their apical endfeet[45]; through their basal process, they guide newly born neurons across the entire thickness of the developing cortex, serving as a central organizer for the assembly of cortical neuronal columns, layers, and circuitry[46-48]. To assess SYNGAP1's function during cortical plate formation, we analyzed 2-month-old haploinsufficient and corrected cortical organoids. At this stage, organoids form robust VZs and the surrounding regions are populated with both upper and deep layer cortical projection neurons[33]. The VZs, which are defined by highly dense Sox2 positive areas, serve as the germinal niche for the organoids; these regions were significantly reduced in size, number, and organization in SYNGAP1 haploinsufficient organoids (Fig. 3a-f) and RGD organoids (Suppl. Fig. 4a-c). The sizable presence of MAP2+ cells within the VZ of haploinsufficient organoids indicates a potentially impaired ability of neuroblasts to migrate away from the ventricular zones towards the cortical plate or an imbalance in direct neurogenesis. This is also consistent with the disorganization of radial glial progenitors seen in SYNGAP1

haploinsufficient rosettes, which are known to serve as migratory scaffolding for neuroblasts *in vivo*. Consistent with previous results, binning analysis of the intermediate progenitor marker Tbr2, the deep layer cortical projection neuron marker Ctip2 and the upper layer cortical projection neuron marker Satb2 (Fig. 3g-h) showed the presence of these neuronal markers in bins closer to the ventricular wall in SYNGAP1 haploinsufficient organoids. This further highlights the role of SYNGAP1 in controlling neuronal positioning and the overall organization of the cortical plate during human neurogenesis.

SYNGAP1 haploinsufficiency impairs the developmental trajectory of hRGCs.

Proper lamination in the developing human cortex is dependent on the precise spatiotemporal regulation of RGCs division and differentiation[49,50]. During ventricular RGC division, mitotic spindle orientation determines the cleavage plane and predicts cell fate decisions that result in either symmetric proliferative or asymmetric differentiative divisions[51,52]. We analyzed the division planes of ventricular radial glia (Fig. 4a) and found an increased proportion of cells undergoing differentiative divisions in haploinsufficient organoids (Fig. 4b-c). This data suggests an earlier depletion of the progenitor pool and potential acceleration of neuronal differentiation.

To analyze this phenotype at higher resolution, we performed single-cell RNA-sequencing analysis on 10663 cells from corrected and haploinsufficient organoids at 4 months. To systematically perform cell type classification, we clustered cells from all organoids and compared signatures of differentially expressed genes with a pre-existing human fetal cortex single cell dataset [53]. This defined 21 main transcriptionally distinct cell types (Figure 4d, Suppl. Fig. 5a; Supplementary Table 5), which included a large diversity of progenitors (cycling cells, radial glia, intermediate progenitor cells) and neuronal cell types (excitatory neurons, corticofugal neurons and callosal projection neurons) representing all the main cell types of the endogenous human fetal cortex.

To determine whether corrected and haploinsufficient organoids can generate the same set of cells, we examined the contribution of each line to the different cell types. Since we had unequal recovery of the number of patient compared to corrected cells, we took a random down sampling

of the corrected cells data set, and compared the distribution of cell types between the two samples (Figure 4e). We found that organoids were highly reproducible in terms of cell type composition; however, the relative percentage of cells contributing to multiple cell types was noticeably different. In haploinsufficient organoids, progenitor cells including cycling RGCs contributed with a lower relative percentage of cells when compared to corrected organoids. In accordance, distinct subtypes of postmitotic neurons were represented in higher proportion in haploinsufficient organoids (Figure 4f).

We next examined the developmental trajectory of the cell types generated within our organoids by pseudotime analysis (Figure 4g). We captured all the relevant cell types in a standard model of human corticogenesis ranging from cycling RGCs to post mitotic Cortical Projection Neuron subtypes (Figure 4g-h, Suppl. Figure 4b). Radial Glia (RG2) and CorticoFugal Projection Neurons (CFuPN), the cell types that mark the beginning and the end of the trajectory, showed an increased distribution of the haploinsufficient cells towards the end point of the trajectory, providing further support for our previous results pointing to accelerated development in the mutant organoids (Figure 4h,i; Suppl. Figure 5c).

Next, to look for networks of genes that vary along this developmental trajectory, we used the graph_test function within the Monocle 3 package and found sets of genes that varied across the different stages from dividing RGCs to intermediate progenitor cells (IPCs) and finally to Callosal Projection Neurons (CPNs) and CFuPNs (Suppl. Figure 5d). We identified a module containing multiple genes associated with radial glia proliferation that was downregulated in mutant organoids (Figure 4i). Progenitor Differentiation and Neuronal Maturation modules (Figure 4 j,k) were instead positively correlated with pseudotime progression and upregulated in haploinsufficient organoids.

Overall, this data suggests that SYNGAP1 controls the timing of radial glial differentiation. SYNGAP1 haploinsufficiency leads to depletion of the progenitor pool coupled with an increase in the number and maturity of cortical projection neurons.

SYNGAP1 haploinsufficient organoids exhibit accelerated maturation of cortical projection neurons.

As additional evidence of the accelerated developmental trajectory in haploinsufficient organoids, we analyzed structural and functional features of neurons in intact 4-month-old organoids. Structural analysis of dendritic complexity in individual neurons showed a more developed dendritic tree arborization with an increase in the number of dendrites in haploinsufficient organoids (Fig. 5a,b). The higher degree of complexity in dendritic arborization was also supported by the scRNA-seq data, showing in CFuPNs an upregulation of transcripts related to the functional categories of neuronal projection regulation and axon development including genes such as CNTN1, DCX, MAP3K13 and SYT4 (Fig. 5c-d). CPNs showed enrichment in the transcription of genes including DCX, NRNX1 and PLXNA2 with an overall upregulation of genes regulating neuronal projection morphogenesis and axon development (Fig. 5e-f). SLITRK5, a gene encoding for a protein known to suppress neurite outgrowth, was found to be downregulated, further supporting evidence of increased dendritic complexity.

Functional neuronal maturation was monitored through recording of spontaneous neuronal activity using an Adeno-Associated Virus driving GCaMP6f as a proxy of intracellular calcium dynamics. Corrected organoids displayed limited spontaneous basal calcium waves; however, haploinsufficient organoids showed an increase in network bursts, with faster transients, and coordinated bursts across distant GCaMP-positive soma (Fig. 5g-l, Suppl. Video 3,4). Action potential (AP) generation and propagation were specifically blocked by tetrodotoxin (TTX), a voltage-gated sodium channel antagonist, and AP firing rate was found to be increased after bath application of glutamate, indicating that registered calcium waves are a result of glutamatergic synaptic connections (Fig. 5m,n). In line with previous evidence[54], these results indicate that haploinsufficient organoids exhibit higher levels of spontaneous activity and a more mature synchronized network.

Collectively, these data show that SYNGAP1 expression in hRGCs is required for precise control of the structural integrity and organization of the VZ, timing of neurogenesis, and cortical lamination. Finally, SYNGAP1 haploinsufficiency ultimately results in an accelerated developmental trajectory of hRGCs.

Discussion

Many human genetic studies of neurodevelopmental diseases including ASD have found enrichment of mutations in genes encoding classically defined synaptic proteins [1,9,55-60]. Currently, most studies of SYNGAP1 and other synaptic proteins have been done within the context of mature synapses in rodent models [23]. Indeed, the lack of a reliable model to study the stage-specific functions of ASD risk genes during human brain development has limited our understanding of their role to rudimentary functional categories. Here, we leveraged 3D human brain organoids to perform longitudinal modeling and functional characterization of SYNGAP1, a top risk gene for ASD in the functional category of synaptic function. We detected SYNGAP1 in hRGCs and identified it as a key regulator of human cortical neurogenesis.

One advantage of using cultures of human cortical organoids is that, at early stages, they are composed by a relatively pure population of cortical progenitors. Analysis of the SYNGAP1 interactome within this population suggests an association between SYNGAP1 and the tight junction protein TJP1, which is a PDZ domain containing protein belonging to the MAGUK family. In neurons, SYNGAP1's interaction with MAGUK proteins is key for protein localization within the PSD machinery[16-18] .Our results suggest a similar role of TJP1 in localizing SYNGAP1 function in the apical domain of radial glial progenitors. SYNGAP1 might regulate cytoskeletal organization in hRGCs through its RASGAP domain and its localization and assembly in macromolecular complexes through its PDZ ligand domain. This is particularly intriguing when considering the critical role of tight junctions and their association with the cytoskeleton in forming and preserving the apical junctional belt, which maintains radial glial apico-basal polarity and neuroepithelial cohesion [45]. As apical radial glial begin to differentiate, there is a downregulation of junctional proteins and a constriction of the apical junctional ring, which enables detachment from the ventricular wall and migration away from the VZ[61]. The disruption of junctional complexes regulating this delamination process has been shown to result in the collapse of apical RGCs morphology, disruption of the ventricular surface, and cortical lamination defects due to failed neuronal migration[62-65]. These phenotypes are consistent with several of our findings in SYNGAP1 haploinsufficient organoids, including disrupted ventricle formation and cortical lamination and the accelerated developmental trajectory of radial glial progenitors. Consistent with the high penetrance of pathogenic SYNGAP1 variants in patients, this phenotype was detected

across two different genetic backgrounds and two different mutations.

A growing body of literature suggests that a dysregulated neurogenesis program may lead to impaired neuronal wiring. This is because establishing proper neuronal circuits requires the spatiotemporally precise control of neuronal positioning, neurogenesis, and afferent and efferent synaptic connectivity[66,67]. Therefore, the impairment in neuronal excitability observed in SYNGAP1 patients may in part be explained by a disruption in microcircuit formation, driven by an altered developmental trajectory of cortical progenitors. Thus, our finding that cortical projection neurons in SYNGAP1 haploinsufficient organoids display accelerated development reshapes the current framework for therapeutic interventions, which could target not only the well-known alterations in synaptic transmission, but also the early developmental defects. The dual function of SYNGAP1 in progenitors and neuronal synapses underscores the importance of dissecting the role of ASD risk genes in specific cell types across developmental stages, and suggests that a similarly nuanced approach may have broader relevance for studying other neurodevelopmental disorders (NDD). This is even more important considering that alterations in developmental trajectories during cortical neurogenesis are emerging as major contributors to the etiology of autism[2-8].

In addition, human genetic studies have found enrichment of mutations in genes encoding PSD proteins [1,9,55,56,58-60], which generally form large protein interaction networks that are considered risk factors for NDD [40,68,69] . In the synapses of the adult mouse brain, SYNGAP1 is a major hub in the PSD PIN, and proteins associated with NDD are SYNGAP1 protein interactors [68,69]. We have found expression of multiple components of the postsynaptic density in our proteomic analysis and shown that some of these proteins are interactors of SYNGAP1 in cortical progenitors. It is tempting to speculate that the complex controlling structural integrity at the PSD of excitatory neurons is also important in regulating the scaffolding properties of hRGCs. Future studies are imperative for characterizing whether disrupting proteins classically considered important for maintenance of the PSD scaffold in neurons may represent a point of convergence for NDD.

Materials and Methods

hiPSC Line Generation

SYNGAP1 p.Q503X and Corrected Cell Line

iPSCs were generated using episomal expression of yamanaka factors in patient-derived PBMCs[70]. A sgRNA targeting the patient-specific mutation in *SYNGAP1* was cloned into pSpCas9(BB)-2A-Puro (PX459) V2.0 (Addgene plasmid #62988). This, along with an HDR template containing the WT *SYNGAP1* sequence, were nucleofected into the patient-derived iPSC line. Individual iPSC colonies were transferred to 24 well plates and subsequently underwent restriction enzyme-based genotyping. Positive colonies were then confirmed via Sanger sequencing and expanded in culture.

HDR Template:

CCGCGAGAACACGCTTGCCACTAAAGCCATAGAAGAGTATATGAGACTGATTGGTCAGAAATATCTCAAGGATGCCATTGGTATGGCCCACACTCAGGCCCTCTTCTTCCCAAACCTGCCA

The underlined CAG sequence corresponds to the insertion of the wt "T" base pair and the underlined T base corresponds to a silent mutation to disrupt the PAM sequence of the sgRNA

The substitution of the truncating "T" with the WT "C" base pair was screen for via restriction enzyme digestion and then confirmed via sanger sequencing.

Mutation – c.1507C>T; p.Q503X nonsense mutation

Genotyping info – Introduction of correction destroys DrdI restriction enzyme site which was used for initial screening of cell lines

RASGAP Dead Line

A sgRNA targeting the arginine finger region of SYNGAP1 was cloned into pSpCas9(BB)-2A-Puro (PX459) V2.0 (Addgene plasmid #62988). This, along with an HDR template to introduce the R485P RasGAP-dead mutation[71], were nucleofected in the 03231 control iPSC line derived from a healthy 56-year-old male[72]. Individual iPSC colonies were transferred to 24 well plates and subsequently underwent restriction enzyme-based genotyping. Positive colonies were subsequently confirmed via Sanger sequencing. Guide Sequence used: CGTGTTCTCGCGGAATATGHDR Template used:

ACTTCCTTTCAGACATGGCCATGTCTGAGGTAGACCGGTTCATGGAACGGGAGCACtTaATATTCCcCGAGAACACGCTTGCCACTAAAGCCATAGAAGAGTATATGAGACTGA

TTGGTCAGA. The introduction of silent PAM mutation creates a new MseI restriction enzyme site which was used for initial screening of cell lines.

03231/SYNGAP1 p.Q503X

The SYNGAP1 p.Q503X cell line was generated in the 03231 control iPSC line derived from a healthy 56-year-old male[72]. Via substitution of c.1507C>T; p.Q503X. A sgRNA targeting the SYNGAP1 c.1507C site was cloned into pSpCas9(BB)-2A-Puro (PX459) V2.0 (Addgene plasmid #62988). The sgRNA together with the HDR template to introduce the 1507C>T mutation. were nucleofected in the 03231 control iPSC line derived from a healthy 56-year-old male[72]. Individual iPSC colonies were transferred to 24 well plates and subsequently underwent restriction enzyme-based genotyping. Positive colonies were subsequently confirmed via Sanger sequencing. Guide Sequence used: CCATACCAATGGCATCCTTG.

HDR template used: CCGCGAGAACACGCTTGCCACTAAAGCCATAGAAGAGTATATG AGACTGATTGGTTAGAAATATCTCAAGGATGCCATTGGTATGGCCCACACTCAGGCC CTCTTCTTCCCAAACCTGCCA

The Underlined TAG region shows the 1507C>T inserted mutation and the underlined T base shows the introduced silent PAM site.

Genotyping info – Introduction of correction modifies the DrdI restriction enzyme site which was used for initial screening of cell lines

Cell Culture and Dorsal Forebrain Organoid Generation

hiPSC lines were maintained with daily media change in mTeSR (STEMCELL Technologies, #85850) on 1:100 geltrex (GIBCO, #A1413301) coated tissue culture plates (CELLTREAT, #229106) and passaged using ReLeSR (STEMCELL Technologies, #100-0484). Cells were maintained below passage 50 and periodically karyotyped via the G-banding Karyotype Service at Children's Hospital Los Angeles. Organoid generation was performed as previously described in[33].

Procurement of Human Tissue

The de-identified human specimen was collected from autopsy, with previous patient consent to institutional ethical regulations of the University of California San Francisco Committee on

Human Research. Collection was at a postmortem interval (PMI) of less than 24 hours. Tissue was collected at the following institution with previous patient consent to institutional ethical regulations: (1) The University of California, San Francisco (UCSF) Committee on Human Research. Protocols were approved by the Human Gamete, Embryo and Stem Cell Research Committee (Institutional Review Board GESCR# 10- 02693) at UCSF. Specimens were evaluated by a neuropathologist as control samples. Tissues were cut coronally, and 1 mm tissue blocks were fixed with 4% paraformaldehyde for two days, and cryoprotected in a 30% sucrose gradient. The tissue was then frozen in OCT and blocks were cut at 30 um with a cryostat and mounted onto glass slides.

Singular Neural Rosette Tissues

All pluripotent lines were maintained in Essential Eight medium (E8) (Thermo Fisher, #A1517001) on geltrex (GIBCO, #A1413301) coated tissue culture plates and routinely passaged with ReLeSR (STEMCELL Technologies, #05872). RGCs derivation from hPSCs was performed using Essential Six Medium (E6) (Thermo Fisher, #A1516501)[73]. To generate RGCs-derived micropatterned, cells were first rinsed with PBS, dissociated with Accutase (STEMCELL Technologies, #07922) for 5 min at 37°C, and collected via centrifugation at 1000 rpm for 5 min. Singularized RGCs were re-suspended in E6 media with 10 µM ROCK inhibitor (Y27632; STEMCELL Technologies, #72302) and seeded onto micropatterned substrates at 75,000 cells/cm2 in 2 mL of media per well. The following day, the media was replaced with 2 mL of E6 media, and 50% media changes were performed daily thereafter. 96-well plates were custom made with micropatterning of poly(ethylene glycol methyl ether)-grafted substrates, presenting arrays of 250µm diameter circular regions and coated with Matrigel over-night[42].

Immunohistochemistry

Organoids were fixed in 4% PFA for 30 min at room temperature before an overnight incubation at 4℃ in 30% sucrose solution. Organoids were then embedded in Tissue-Tek O.C.T. compound (Sakura, #62550) and sectioned at 20 µm with a cryostat onto glass slides (Globe Scientific, #1354W). Slides were washed 3x with a 0.1% Tween20 (Sigma, #P9416) solution before a 1-hour incubation in 0.3%TritonX-100 (Sigma, #T9284) and 6% bovine serum albumin (Sigma, #AA0281) solution. An overnight incubation at 4℃ in a primary antibody solution was followed

by a 2-hour room temperature incubation in a secondary antibody solution, both consisting of 0.1%TritonX-100 and 2.5%BSA with 3 washes before and after secondary antibody incubation. Slides were coverslipped using Fluoromount G (EMS, #50-259-73).

Antibody	**Species**	**Catalog Number**	**Company**
DAPI	--	80051-386	Sigma/Millipore
SATB2	Mouse	AB51502	Abcam
MAP2	Chicken	AB5392	Abcam
NESTIN	Mouse	AB22035	Abcam
CTIP2 (BLC11B)	Rat	AB18465	Abcam
SOX2	Goat	AF2018	RD Systems
TBR2 (EOMES)	Rabbit	AB2283	Millipore
PAX6	Rabbit	901301	Biolegend
N-CAD	Rabbit	22018-1-AP	Protientech
Ki67	Rabbit	ab15580	AbCam
Phospho-Histone H3	Mouse	#9706	Cell Signaling technology
Pericentrin	Rabbit	ab4448	AbCam
N-cadherin	Mouse	610920	BD
Anti-RFP	Rabbit	600-401-379	Rockland
p-Vimentin	Mouse		MBL
Anti-GFP	Chicken	G160	Abm

ZO-1 (TJP1)	Mouse	610966	BD Transduction Laboratories
Alexa Fluor 647 Phalloidin	--	A30107	Thermo Scientific
SYNGAP1	Rabbit	5539	Cell Signaling Technology
Acetylated Tubulin	Mouse	T6793-100UL	Sigma Aldrich
Nestin	Mouse	ab22035	AbCam

Whole proteome analysis of organoids

Deep proteome profiling was performed on 21 human cortical organoids at D.I.V. 7. After lysis in RIPA buffer (Pierce), extracted proteins were reduced with 5 mM DTT, followed by incubation with 20 mM iodoacetamide in the dark. Sample cleanup was performed using the SP3 method [74] and on-bead digestion was performed overnight using Trypsin/Lys-C (Promega). Eluted tryptic peptides from SP3 beads were pre-fractionated by high pH reverse phase chromatography into 96 individual fractions using a 64-minute gradient from 1% to 50% solvent B (A: 10mM NH_4OH, B: acetonitrile) on a Cadenza C18 column (Imtakt) The collected 96 fractions were recombined into final 24 fractions by pooling every 24th fraction for LC-MS/MS analysis. 500 ng peptide from each fraction was analyzed by a 60-minute LC/MS/MS method on an Orbitrap Fusion Lumos mass spectrometer (ThermoFisher Scientific) interfaced with a Ultimate 3000 UHPLC system (ThermoFisher Scientific). Full scans were acquired in the Orbitrap at a resolution of 120K and a scan range of 400-1600 m/z. Most abundant precursor ions from the full scan were selected using an isolation window of 1.6 Da and subjected to HCD fragmentation with an NCE of 30% and detection in the iontrap. Raw data files were searched using Byonic (v2.16.11) in Proteome Discoverer (v2.4) against the Swissprot human protein database (downloaded November, 2020). The following search parameters were used: fully tryptic peptides with a maximum of 2 missed cleavages, 10 ppm precursor mass tolerance, 0.5 Da fragment mass tolerance, fixed modification of cysteine carbamidomethylation, oxidation of methionine, deamidation of glutamine and asparagine were selected as dynamic modifications. The protein and peptide-level confidence thresholds were set at 99% (FDR <0.01). Using this pipeline, we identified a total of 8686 proteins,

including 24 unique peptides for SYNGAP1. The protein/gene list obtained from MS analysis was imported into SynGO portal and cellular component annotation where obtained.

Generation and Analysis of the SYNGAP1 Interactome

We immuno-isolated SYNGAP1 protein in human cortical organoids at D.I.V. 7, generated from the 03231 control iPSC line, following the same experimental pipeline used in Wilkinson et al; 2019. In addition, we identified 135 proteins corresponding to the SYNGAP1 interactome. Positive interactors were identified by 2 different peptides in duplicate assays, not present in the SYNGAP1 knockout control.

Identification of the SYNGAP1 alpha 1 isoform

Digested and desalted immunoprecipitated samples were analyzed using a 60-minute method on an Orbitrap Fusion Lumos mass spectrometer coupled to an Ultimate 3000 liquid chromatograph with a 50 cm C18 column (ThermoFisher Scientific EasySpray column, 75 µM ID, 2 µm particle size). Mass spectrometry data was acquired using a combined data dependent MS/MS experiment and targeted measurement of SYNGAP1 alpha 1 isoform peptides. In the data-dependent acquisition mode, full scans were acquired in the Orbitrap at a resolution of 120K and a scan range of 400-1600 m/z. Most abundant precursor ions from the full scan were selected using an isolation window of 1.6 Da and subjected to HCD fragmentation with NCE of 35% and detection in the iontrap. In addition, selected precursors of SYNGAP1 alpha 1 isoform specific peptides were measured by Parallel Reaction Monitoring (PRM). PRM scans were performed in the Orbitrap at 30K resolution following HCD fragmentation (35% NCE) of precursors at m/z 358.20 (retention time window of 13-17 minutes) and m/z 651.8331 (retention time window of 38.3-46.3 minutes). Data Analysis: Data were searched against the Human Swissprot database using Mascot v2.6 run within Proteome Discoverer v2.4. Search parameters included: fully tryptic peptides with a maximum of 2 missed cleavages, fixed modification of carbamidomethylation of cysteine, and dynamic modification of methionine oxidation. Data was filtered at a 1% target/decoy FDR at the peptide and protein level. PRM data was quantified using Skyline [75]. Annotated peptide spectra were generated using Interactive Peptide Spectral Annotator[76].

Bulk-RNA Sequencing

Organoids derived from haploinsufficient and corrected control lines were collected at DIV 7 from 3 independent differentiations (50 corrected and 100 patient organoids per genotype, per differentiation). Total RNA was isolated using Qiagen columns. Library preparation and RNA sequencing were performed as a service by QuickBiology.

Data preprocessing was performed with *trimmomatic* to filter out adapter sequences and low-quality reads. The processed reads were mapped to the human reference genome from Ensembl (GRCh38.p13) using *HISAT2 v2.1.0*. We summed the read counts and TPM of all alternative splicing transcripts of a gene to obtain gene expression levels and restricted our analysis to 20000 expressed genes with an average TPM >1 in each sample. Differential expression analysis was performed with the *DESeq2 package* (v1.20.0). The following cutoffs values were used for assigning differentially expressed genes (DEGs): P-adjusted value < 0.05, false discovery rate (FDR) < 0.05 and |log2FC| ≥ 0.6. We obtained a list of both upregulated and downregulated DEGs between SYNGAP1+/- and control organoids. ClusterProfiler software (v.4.2.2) was used to perform functional annotations of the DEGs, according to Gene Ontology (GO) categories (biological process, molecular function and cellular components). Using these gene lists, we searched the Panther GO-Slim Biological Processes ontology database using a statistical overrepresentation test (FDR, P < 0.05).

Single Cell Dissociation

7-day-old organoids were rinsed with 1X PBS (Corning, #21-040-CV) and incubated at 37°C for 15 min with 1x TripLE Express Enzyme (Thermo Fisher Scientific, #12-605-010). Organoids were dissociated by pipetting up and down with a 1000 µl pipette followed by 200 µl pipette until a single cell resuspension was obtained. Cells were plated onto 1:100 geltrex coated round plastic coverslips (Thermo Fisher Scientific, #NC0706236) at a density of 15800 cells/cm^2.

Single Cell Dissociation for scRNA-Sequencing

Organoids were dissociated as previously described[30,51]. Briefly, 3-4 pooled organoids at 3-4 months of age from both haploinsufficient and corrected lines were transferred to a 60 mm dish containing a papain and DNase solution from the Papain Dissociation Kit (Worthington, #LK003150). Organoids were minced into small bits with razors and incubated for 30 min at 37°C

on an orbital shaker, then mixed with a 1ml tip several times and returned for another 5-10 min at 37ºC. Next, the pieces were triturated 5-10 times with a 10 ml pipet and transferred to a 15 ml conical tube containing 8 ml final Inhibitor solution and DNase. The tube was inverted a few times and left upright for a few minutes for larger debris (if any) to settle, then the single cell suspension was transferred to a new conical tube, and centrifuge for 7 min at 300 g. The cell pellet was resuspended in 500 ul to 1 ml of 0.04% BSA/PBS and passed through a 0.4 micron filter basket and counted. The solution was then adjusted to a target concentration of 1000 cells/µl.

Sequencing Analysis, Quality Control (QC), and Clustering

10X Genomic scRNA sequencing was performed by the USC Molecular Genomics Core Facility. Samples were processed on the 10x Single Cell Gene Expression 3' v3.1 kit. Raw sequencing reads were aligned with the human reference genome (GRCh38-2020-A) via the CellRanger (v6.0.2) pipeline to generate a cell-by-gene count matrix. We recovered 3463 patient and 7968 corrected cells for a total of 11416 cells. Next, we used Seurat (v4.0.1 using R v4.0.) to perform initial QC with standard cutoffs of min.cells = 3, min.features = 200, mitochondrial percentage (<15%), and removal of low complexity cells (nCount < 1250). The regression of the cycling cell genes, normalization, variable features, and scaling were done using the SCTransform function. Principal component analysis (PCA) was performed. Using the FindNeighbors and FindClusters functions (resolution = 0.2, 0.8 and 1.2), clusters of cell types were generated. Resolution 0.8 was used to classify the cells into 21 cell type clusters. Clusters were classified according to known markers and previously identified molecular profiles[32,33], and compared with a human fetal data set[53]. To calculate the DEGs between control and mutant organoids for each cluster, we used the *FindMarker* function with the test.use attribute set to the default Wilcoxon rank sum test.

Pseudotime and Gene Module Analysis

Trajectory and module analysis was performed using Monocle 3 (v.0.2.2 using R v4.0). Taking the SCT normalized data set from previous analysis, we again performed PCA and uniform manifold approximation and projection (UMAP) dimensionality reduction. Since the gene expression matrix was already normalized, further log normalization was not performed in the preprocessing step. Next, we used this low-dimensional space to learn a principal graph to order the cells in pseudotime. For the initial principal graph using all the cells, we ordered the cells, but

set the partition attribute to false. Next, to identify the subset of cells participating in a known trajectory of early cortical neurogenesis, we chose a starting point that represents the earliest developmental cell type, which is the RGCs cluster, and traced a path through IPCs to the CFuPN cluster as the end point. This subset of cells was used for subsequent gene module analysis.

To discover patterns of coordinated gene expression across the cells along this pathway, we implemented the Moran's I test using the *graph_test* function. Next, we used the *find_gene_modules* function to group the genes into modules using Louvain community analysis. To calculate the differential expression of modules, a selected gene module list was passed to the Seurat function *AddModuleScore*. This function calculated the average expression levels of each module on a single cell level. All analyzed features were binned based on averaged expression, and the control features were randomly selected from each bin. Finally, for each module, a Wilcoxon rank sum test was used to compare for significant differences in module score between control versus mutant states.

RFP Labeling

Organoids were transduced with EF1A-RFP lentivirus (Cellomics Technology, # PLV-10072-50). 1 µl of stock virus (1x10^8 TU/ml) was diluted into 500 µl Cortical Differentiation Medium IV (CDMIV, without Matrigel) in a 24-well ultra-low attachment plate (Corning, # 3473) containing a single organoid. After 24 hours of incubation, full media change was performed. 48 hours later, organoids were transferred to a 6-well ultra-low attachment plate (Corning, #3471). 1 week after transduction, organoids were randomly selected for imaging analysis and individually transferred to a u-Slide 8-well Glass-bottom plate (Ibidi, #80827).

Calcium Imaging

Organoids were transduced with pAAV-CAG-SomaGCaMP6f2 (Addgene, #158757) as described in[2]. Four-month-old cortical organoids were randomly selected and transferred to a recording chamber kept at 37 °C using a heating platform and a controller (TC-324C, Warner Instruments) in 5% methyl-cellulose in BrainPhys Imaging Optimized Medium (STEMCELL Technologies, #05796). Imaging was performed using a SP-8X microscope with a multiphoton laser. Time-lapse images were acquired at 1 frame for 860 ms, using a 25x 0.95 NA water objective (2.5 mm WD) and resulting in a view of 200 x 200 µm^2. Basal activity was recorded for 10 mins in each of the 3

randomly selected areas of the imaged organoid. Pharmacological treatment was performed with a bath application of Tetrodotoxin, TTX (Tocris, #1078/1) at a final concentration of 2 µM, and glutamate (Hello Bio, #HB0383) at 100 µM.

Singular Neural Rosette Tissues Analysis

The presence of 0 polarization foci were '0 Rosette'; 1 rosette foci were '1 Rosette'; ≥1 rosette with ≥1 additional polarization foci were '+1 Rosette'.

F-actin Analysis

F-actin Intensity and Anisotropy were analyzed following phalloidin staining on dissociated organoids. DAPI/PAX6/Phalloidin positive cells were selected for confocal imaging. Maximum intensity projection images for the Phalloidin channel were generated with Image-J software. Single cells were selected using a free hand tool in Image-J and analyzed for total intensity. Anisotropy was automatically calculated by using the FibrilTool plugin in Image-J[77].

Morphological Dendrite Analysis

RFP positive organoids were imaged using a 20x objective with the Leica Thunder Microscope. Maximum projection of each organoid was applied, and the number of dendrites per cell was calculated using the Sholl Analysis plugin in Image-J software.

Ventricular Zone Analysis of 2-month-old Organoids

Two-month-old organoids were sectioned and immunostained for SOX2 and DAPI. Only cryosections near the middle of each organoid were used for analysis. The ventricular zone (VZ) was defined by exclusive SOX2 immunoreactivity and neural tube-like morphology. Image-J software was used to analyze the thickness, area, and total number of VZs. The line tool was used to measure the thickness of each VZ (µm); an average of 3 measurements per VZ were considered. The freehand tool was used to trace the entire VZ and measure the total area (μm^2). For each organoid, 3-6 regions of interest (ROI) were defined, and the number of VZs in each Region of Interest (ROI) were counted. For all VZ analyses, 4 independent differentiations and 3 organoids from each differentiation were measured.

The organized versus disorganized analysis of the VZ was based on MAP2 staining. The ventricles with clusters of MAP2 positive cells in the germinal zone were defined as disorganized; the ventricles showing clear boundaries between the cortical and germinal zones were defined as organized. For each line, 3 organoids from 3 independent differentiations were quantified.

The cleavage angle was defined as the angle between the ventricular apical surface and the cleavage plane of dividing cells. Pericentrin and pVimentin were used to stain the centrosome and the dividing RG, respectively, to clearly visualize the cleavage plane. The angle was measured manually with the angle tool in Image-J.

Binning analysis was performed on relatively isolated ventricles to ensure the binning area has no other interfering ventricles. Seven 25x50 μm rectangular bins were stacked vertically starting from the edge of the ventricle and extending to the nearest edge of the organoid. This provided a uniform grid or binning area that was then used as a visual for the layering of specific cell markers including: CTIP2, SATB2, and TBR2. Positive cells for each stain in each of the bins were manually counted and normalized to the total number of DAPI positive cells per bin.

Calcium Imaging Data Analysis

Leica LasX .avi files were exported and analyzed with Image-J software. Conversion in gray scale was performed and ROI were selected with the ROI Manager Tool. Average intensity over the entire length of the recording was obtained for each ROI. Data values were exported in Excel software and $\Delta F/F(t)$, defined as $(F(t) - F_0(t))/F_0(t)$, was calculated. Calcium peak frequency was analyzed using IgorPro 8 software and visualized with QtiPlot software.

Statistical Analysis

Data is shown as mean ± SEM. Statistical analysis was performed using the Graph Pad Prism 6.0. Shapiro-Wilk test was performed to determine the normality of the data (alpha=0.05). Comparisons of means in 2 or more groups were made using an unpaired Student's t-test or analysis of variance (ANOVA). Significant main effects were analyzed further by post hoc comparisons of means using Bonferroni's multiple comparisons test.

References

1 De Rubeis, S. *et al.* Synaptic, transcriptional and chromatin genes disrupted in autism. *Nature* **515**, 209-215, doi:10.1038/nature13772 (2014).

2 Paulsen, B. *et al.* Autism genes converge on asynchronous development of shared neuron classes. *Nature* **602**, 268-273, doi:10.1038/s41586-021-04358-6 (2022).

3 Mariani, J. *et al.* FOXG1-Dependent Dysregulation of GABA/Glutamate Neuron Differentiation in Autism Spectrum Disorders. *Cell* **162**, 375-390, doi:10.1016/j.cell.2015.06.034 (2015).

4 Jourdon, A. *et al.* ASD modelling in organoids reveals imbalance of excitatory cortical neuron subtypes during early neurogenesis. *bioRxiv*, 2022.2003.2019.484988, doi:10.1101/2022.03.19.484988 (2022).

5 Villa, C. E. *et al.* CHD8 haploinsufficiency links autism to transient alterations in excitatory and inhibitory trajectories. *Cell Rep* **39**, 110615, doi:10.1016/j.celrep.2022.110615 (2022).

6 Schafer, S. T. *et al.* Pathological priming causes developmental gene network heterochronicity in autistic subject-derived neurons. *Nat Neurosci* **22**, 243-255, doi:10.1038/s41593-018-0295-x (2019).

7 de Jong, J. O. *et al.* Cortical overgrowth in a preclinical forebrain organoid model of CNTNAP2-associated autism spectrum disorder. *Nat Commun* **12**, 4087, doi:10.1038/s41467-021-24358-4 (2021).

8 Urresti, J. *et al.* Cortical organoids model early brain development disrupted by 16p11.2 copy number variants in autism. *Mol Psychiatry* **26**, 7560-7580, doi:10.1038/s41380-021-01243-6 (2021).

9 Satterstrom, F. K. *et al.* Large-Scale Exome Sequencing Study Implicates Both Developmental and Functional Changes in the Neurobiology of Autism. *Cell* **180**, 568-584.e523, doi:10.1016/j.cell.2019.12.036 (2020).

10 Chen, H. J., Rojas-Soto, M., Oguni, A. & Kennedy, M. B. A synaptic Ras-GTPase activating protein (p135 SynGAP) inhibited by CaM kinase II. *Neuron* **20**, 895-904, doi:10.1016/s0896-6273(00)80471-7 (1998).

11 Kim, J. H., Liao, D., Lau, L. F. & Huganir, R. L. SynGAP: a synaptic RasGAP that associates with the PSD-95/SAP90 protein family. *Neuron* **20**, 683-691, doi:10.1016/s0896-6273(00)81008-9 (1998).

12 Komiyama, N. H. *et al.* SynGAP regulates ERK/MAPK signaling, synaptic plasticity, and learning in the complex with postsynaptic density 95 and NMDA receptor. *J Neurosci* **22**, 9721-9732 (2002).

13 Kim, J. H., Lee, H. K., Takamiya, K. & Huganir, R. L. The role of synaptic GTPase-activating protein in neuronal development and synaptic plasticity. *J Neurosci* **23**, 1119-1124 (2003).

14 Zhu, J. J., Qin, Y., Zhao, M., Van Aelst, L. & Malinow, R. Ras and Rap control AMPA receptor trafficking during synaptic plasticity. *Cell* **110**, 443-455, doi:10.1016/s0092-8674(02)00897-8 (2002).

15 Araki, Y., Zeng, M., Zhang, M. & Huganir, R. L. Rapid dispersion of SynGAP from synaptic spines triggers AMPA receptor insertion and spine enlargement during LTP. *Neuron* **85**, 173-189, doi:10.1016/j.neuron.2014.12.023 (2015).

16 Walkup, W. G. *et al.* A model for regulation by SynGAP-α1 of binding of synaptic proteins to PDZ-domain 'Slots' in the postsynaptic density. *Elife* **5**, doi:10.7554/eLife.16813 (2016).

17 Zeng, M. *et al.* Phase Transition in Postsynaptic Densities Underlies Formation of Synaptic Complexes and Synaptic Plasticity. *Cell* **166**, 1163-1175.e1112, doi:10.1016/j.cell.2016.07.008 (2016).

18 Zeng, M., Bai, G. & Zhang, M. Anchoring high concentrations of SynGAP at postsynaptic densities via liquid-liquid phase separation. *Small GTPases* **10**, 296-304, doi:10.1080/21541248.2017.1320350 (2019).

19 Knuesel, I., Elliott, A., Chen, H. J., Mansuy, I. M. & Kennedy, M. B. A role for synGAP in regulating neuronal apoptosis. *Eur J Neurosci* **21**, 611-621, doi:10.1111/j.1460-9568.2005.03908.x (2005).

20 Su, P. *et al.* Disruption of SynGAP-dopamine D1 receptor complexes alters actin and microtubule dynamics and impairs GABAergic interneuron migration. *Sci Signal* **12**, doi:10.1126/scisignal.aau9122 (2019).

21 Berryer, M. H. *et al.* Mutations in SYNGAP1 cause intellectual disability, autism, and a specific form of epilepsy by inducing haploinsufficiency. *Hum Mutat* **34**, 385-394, doi:10.1002/humu.22248 (2013).

22 Kilinc, M. *et al.* Species-conserved SYNGAP1 phenotypes associated with neurodevelopmental disorders. *Mol Cell Neurosci* **91**, 140-150, doi:10.1016/j.mcn.2018.03.008 (2018).

23 Gamache, T. R., Araki, Y. & Huganir, R. L. Twenty Years of SynGAP Research: From Synapses to Cognition. *The Journal of Neuroscience* **40**, 1596, doi:10.1523/JNEUROSCI.0420-19.2020 (2020).

24 Lancaster, M. A. *et al.* Cerebral organoids model human brain development and microcephaly. *Nature* **501**, 373-379, doi:10.1038/nature12517 (2013).

25 Bershteyn, M. *et al.* Human iPSC-Derived Cerebral Organoids Model Cellular Features of Lissencephaly and Reveal Prolonged Mitosis of Outer Radial Glia. *Cell Stem Cell* **20**, 435-449.e434, doi:10.1016/j.stem.2016.12.007 (2017).

26 Kanton, S. *et al.* Organoid single-cell genomic atlas uncovers human-specific features of brain development. *Nature* **574**, 418-422, doi:10.1038/s41586-019-1654-9 (2019).

27 Klaus, J. *et al.* Altered neuronal migratory trajectories in human cerebral organoids derived from individuals with neuronal heterotopia. *Nat Med* **25**, 561-568, doi:10.1038/s41591-019-0371-0 (2019).

28 Esk, C. *et al.* A human tissue screen identifies a regulator of ER secretion as a brain-size determinant. *Science* **370**, 935-941, doi:10.1126/science.abb5390 (2020).

29 Khan, T. A. *et al.* Neuronal defects in a human cellular model of 22q11.2 deletion syndrome. *Nat Med* **26**, 1888-1898, doi:10.1038/s41591-020-1043-9 (2020).

30 Samarasinghe, R. A. *et al.* Identification of neural oscillations and epileptiform changes in human brain organoids. *Nat Neurosci* **24**, 1488-1500, doi:10.1038/s41593-021-00906-5 (2021).

31 Tidball, A. M. *et al.* Self-organizing Single-Rosette Brain Organoids from Human Pluripotent Stem Cells. *bioRxiv*, 2022.2002.2028.482350, doi:10.1101/2022.02.28.482350 (2022).

32 Quadrato, G. *et al.* Cell diversity and network dynamics in photosensitive human brain organoids. *Nature* **545**, 48-53, doi:10.1038/nature22047 (2017).

33 Velasco, S. *et al.* Individual brain organoids reproducibly form cell diversity of the human cerebral cortex. *Nature* **570**, 523-527, doi:10.1038/s41586-019-1289-x (2019).

34 Camp, J. G. *et al.* Human cerebral organoids recapitulate gene expression programs of fetal neocortex development. *Proc Natl Acad Sci U S A* **112**, 15672-15677, doi:10.1073/pnas.1520760112 (2015).

35 Trevino, A. E. *et al.* Chromatin accessibility dynamics in a model of human forebrain development. *Science* **367**, doi:10.1126/science.aay1645 (2020).

36 Gordon, A. *et al.* Long-term maturation of human cortical organoids matches key early postnatal transitions. *Nat Neurosci* **24**, 331-342, doi:10.1038/s41593-021-00802-y (2021).

37 Michaelson, S. D. *et al.* SYNGAP1 heterozygosity disrupts sensory processing by reducing touch-related activity within somatosensory cortex circuits. *Nat Neurosci* **21**, 1-13, doi:10.1038/s41593-018-0268-0 (2018).

38 Aceti, M. *et al.* Syngap1 haploinsufficiency damages a postnatal critical period of pyramidal cell structural maturation linked to cortical circuit assembly. *Biol Psychiatry* **77**, 805-815, doi:10.1016/j.biopsych.2014.08.001 (2015).

39 Eze, U. C., Bhaduri, A., Haeussler, M., Nowakowski, T. J. & Kriegstein, A. R. Single-cell atlas of early human brain development highlights heterogeneity of human neuroepithelial cells and early radial glia. *Nat Neurosci* **24**, 584-594, doi:10.1038/s41593-020-00794-1 (2021).

40 Li, J. *et al.* Spatiotemporal profile of postsynaptic interactomes integrates components of complex brain disorders. *Nat Neurosci* **20**, 1150-1161, doi:10.1038/nn.4594 (2017).

41 Araki, Y. *et al.* SynGAP isoforms differentially regulate synaptic plasticity and dendritic development. *Elife* **9**, doi:10.7554/eLife.56273 (2020).

42 Knight, G. T. *et al.* Engineering induction of singular neural rosette emergence within hPSC-derived tissues. *Elife* **7**, doi:10.7554/eLife.37549 (2018).

43 Carlisle, H. J., Manzerra, P., Marcora, E. & Kennedy, M. B. SynGAP regulates steady-state and activity-dependent phosphorylation of cofilin. *J Neurosci* **28**, 13673-13683, doi:10.1523/JNEUROSCI.4695-08.2008 (2008).

44 Tomoda, T., Kim, J. H., Zhan, C. & Hatten, M. E. Role of Unc51.1 and its binding partners in CNS axon outgrowth. *Genes Dev* **18**, 541-558, doi:10.1101/gad.1151204 (2004).

45 Aaku-Saraste, E., Hellwig, A. & Huttner, W. B. Loss of occludin and functional tight junctions, but not ZO-1, during neural tube closure--remodeling of the neuroepithelium prior to neurogenesis. *Dev Biol* **180**, 664-679, doi:10.1006/dbio.1996.0336 (1996).

46 Edmondson, J. C. & Hatten, M. E. Glial-guided granule neuron migration in vitro: a high-resolution time-lapse video microscopic study. *J Neurosci* **7**, 1928-1934 (1987).

47 Rakic, P. Guidance of neurons migrating to the fetal monkey neocortex. *Brain Res* **33**, 471-476, doi:10.1016/0006-8993(71)90119-3 (1971).

48 Rakic, P. Mode of cell migration to the superficial layers of fetal monkey neocortex. *J Comp Neurol* **145**, 61-83, doi:10.1002/cne.901450105 (1972).

49 Rakic, P. Neuronal migration and contact guidance in the primate telencephalon. *Postgrad Med J* **54 Suppl 1**, 25-40 (1978).

50 Nowakowski, T. J., Pollen, A. A., Sandoval-Espinosa, C. & Kriegstein, A. R. Transformation of the Radial Glia Scaffold Demarcates Two Stages of Human Cerebral Cortex Development. *Neuron* **91**, 1219-1227, doi:10.1016/j.neuron.2016.09.005 (2016).

51 Chenn, A. & McConnell, S. K. Cleavage orientation and the asymmetric inheritance of Notch1 immunoreactivity in mammalian neurogenesis. *Cell* **82**, 631-641, doi:10.1016/0092-8674(95)90035-7 (1995).

52 Shitamukai, A., Konno, D. & Matsuzaki, F. Oblique radial glial divisions in the developing mouse neocortex induce self-renewing progenitors outside the germinal zone that resemble primate outer subventricular zone progenitors. *J Neurosci* **31**, 3683-3695, doi:10.1523/JNEUROSCI.4773-10.2011 (2011).

53 Nowakowski, T. J. *et al.* Spatiotemporal gene expression trajectories reveal developmental hierarchies of the human cortex. *Science* **358**, 1318-1323, doi:10.1126/science.aap8809 (2017).

54 Llamosas, N. *et al.* SYNGAP1 Controls the Maturation of Dendrites, Synaptic Function, and Network Activity in Developing Human Neurons.

55 Fromer, M. *et al.* De novo mutations in schizophrenia implicate synaptic networks. *Nature* **506**, 179-184, doi:10.1038/nature12929 (2014).

56 Genovese, G. *et al.* Increased burden of ultra-rare protein-altering variants among 4,877 individuals with schizophrenia. *Nat Neurosci* **19**, 1433-1441, doi:10.1038/nn.4402 (2016).

57 Kirov, G. *et al.* De novo CNV analysis implicates specific abnormalities of postsynaptic signalling complexes in the pathogenesis of schizophrenia. *Mol Psychiatry* **17**, 142-153, doi:10.1038/mp.2011.154 (2012).

58 O'Roak, B. J. *et al.* Exome sequencing in sporadic autism spectrum disorders identifies severe de novo mutations. *Nat Genet* **43**, 585-589, doi:10.1038/ng.835 (2011).

59 O'Roak, B. J. *et al.* Sporadic autism exomes reveal a highly interconnected protein network of de novo mutations. *Nature* **485**, 246-250, doi:10.1038/nature10989 (2012).

60 Peça, J. & Feng, G. Cellular and synaptic network defects in autism. *Curr Opin Neurobiol* **22**, 866-872, doi:10.1016/j.conb.2012.02.015 (2012).

61 Kawaguchi, A. Neuronal Delamination and Outer Radial Glia Generation in Neocortical Development. *Frontiers in Cell and Developmental Biology* **8** (2021).

62 Kadowaki, M. *et al.* N-cadherin mediates cortical organization in the mouse brain. *Dev Biol* **304**, 22-33, doi:10.1016/j.ydbio.2006.12.014 (2007).

63 Cappello, S. *et al.* A radial glia-specific role of RhoA in double cortex formation. *Neuron* **73**, 911-924, doi:10.1016/j.neuron.2011.12.030 (2012).

64 Gil-Sanz, C., Landeira, B., Ramos, C., Costa, M. R. & Müller, U. Proliferative defects and formation of a double cortex in mice lacking Mltt4 and Cdh2 in the dorsal telencephalon. *J Neurosci* **34**, 10475-10487, doi:10.1523/JNEUROSCI.1793-14.2014 (2014).

65 Yoon, K. J. *et al.* Modeling a genetic risk for schizophrenia in iPSCs and mice reveals neural stem cell deficits associated with adherens junctions and polarity. *Cell Stem Cell* **15**, 79-91, doi:10.1016/j.stem.2014.05.003 (2014).

66 Noctor, S. C., Martínez-Cerdeño, V., Ivic, L. & Kriegstein, A. R. Cortical neurons arise in symmetric and asymmetric division zones and migrate through specific phases. *Nat Neurosci* **7**, 136-144, doi:10.1038/nn1172 (2004).

67 He, S., Li, Z., Ge, S., Yu, Y. C. & Shi, S. H. Inside-Out Radial Migration Facilitates Lineage-Dependent Neocortical Microcircuit Assembly. *Neuron* **86**, 1159-1166, doi:10.1016/j.neuron.2015.05.002 (2015).

68 Coba, M. P. *et al.* Dlgap1 knockout mice exhibit alterations of the postsynaptic density and selective reductions in sociability. *Sci Rep* **8**, 2281, doi:10.1038/s41598-018-20610-y (2018).
69 Li, J. *et al.* Long-term potentiation modulates synaptic phosphorylation networks and reshapes the structure of the postsynaptic interactome. *Sci Signal* **9**, rs8, doi:10.1126/scisignal.aaf6716 (2016).
70 Okita, K. *et al.* An efficient nonviral method to generate integration-free human-induced pluripotent stem cells from cord blood and peripheral blood cells. *Stem Cells* **31**, 458-466, doi:10.1002/stem.1293 (2013).
71 Klose, A. *et al.* Selective disactivation of neurofibromin GAP activity in neurofibromatosis type 1. *Hum Mol Genet* **7**, 1261-1268, doi:10.1093/hmg/7.8.1261 (1998).
72 Wilkinson, B. *et al.* Endogenous Cell Type-Specific Disrupted in Schizophrenia 1 Interactomes Reveal Protein Networks Associated With Neurodevelopmental Disorders. *Biol Psychiatry* **85**, 305-316, doi:10.1016/j.biopsych.2018.05.009 (2019).
73 Lippmann, E. S., Estevez-Silva, M. C. & Ashton, R. S. Defined human pluripotent stem cell culture enables highly efficient neuroepithelium derivation without small molecule inhibitors. *Stem Cells* **32**, 1032-1042, doi:10.1002/stem.1622 (2014).
74 Hughes, C. S. *et al.* Single-pot, solid-phase-enhanced sample preparation for proteomics experiments. *Nat Protoc* **14**, 68-85, doi:10.1038/s41596-018-0082-x (2019).
75 Pino, L. K. *et al.* The Skyline ecosystem: Informatics for quantitative mass spectrometry proteomics. *Mass Spectrom Rev* **39**, 229-244, doi:10.1002/mas.21540 (2020).
76 Brademan, D. R., Riley, N. M., Kwiecien, N. W. & Coon, J. J. Interactive Peptide Spectral Annotator: A Versatile Web-based Tool for Proteomic Applications. *Mol Cell Proteomics* **18**, S193-S201, doi:10.1074/mcp.TIR118.001209 (2019).
77 Boudaoud, A. *et al.* FibrilTool, an ImageJ plug-in to quantify fibrillar structures in raw microscopy images. *Nat Protoc* **9**, 457-463, doi:10.1038/nprot.2014.024 (2014).

Acknowledgments: We thank the Syngap Research Fund and families participating in this study for their collaboration. We thank the Pediatric Neuropathology Research Lab (PNRL) of UCSF and honor the families who generously donated the tissue samples used in this study.

We thank Dr. Paola Arlotta, Dr. Fiona Francis, current and former members of the Quadrato lab for insightful discussions and feedback on this project. We thank Cristy Lytal for editing the manuscript.

We thank Seth Walter Ruffins and the Optical Imaging Facility at USC for providing guidance and support of imaging analyses. We thank Christopher Taitano-Johnson, Thomas Rintoul and Angela Albanese for outstanding technical support.

Funding: This work was supported by the Donald D. and Delia B. Baxter Foundation, the Edward Mallinckrodt Jr. Foundation and National Science Foundation 5351784498, the Eli and Edythe Broad Foundation to G.Q. This work was supported in part by NIH grants from the National Institute of Mental Health to M.P.C: MH115005
This reported research includes work performed in the mass spectrometry core supported by the National Cancer Institute of the National Institutes of Health under grant number P30CA033572. The content is solely the responsibility of the authors and does not necessarily represent the official views of the National Institutes of Health.

Author contributions M.B., A.D., T.N., M.P.C., and G.Q. conceived the experiments. M.B and A.D. generated, cultured, and characterized single rosette cultures; J.P.U. performed live imaging of single rosettes; G.K. and R.S.A. prepared single rosette culture substrates; M.B, A.D., and T.X. generated, cultured, and characterized all of the organoids used in this study. A.D. performed scRNA-seq and bulk RNA-seq experiments with help from T.X. and T.N.; T.N. performed scRNA-seq analysis and worked on cell type assignments and data analysis; T.X. performed bulk scRNA-seq analysis. B.W. performed sample preparation for Proteomic analysis, and R.M., R.S., P.P. performed analysis of the proteomic data under the supervision of M.P.C.; M.B. performed the calcium imaging experiments and analysis; B.W. designed and generated the SYNGAP1 p.Q503X, corrected, RGD, and 03231/SYNGAP1 P.Q503X -edited lines under the supervision of M.P.C.. E.H. prepared and provided human fetal tissue. G.Q. supervised all aspects of the project; M.B., A.D., and G.Q. wrote the manuscript with contributions from all authors.

Competing interests: G.K. and R.S.A are inventors on U.S. Patent App. No. 16/044236 that describes methods for generating microarrayed single rosette cultures, and they are co-founders of Neurosetta LLC that is focused on commercializing the culture platform.

Data and materials availability:

Bulk RNA Seq Raw Counts https://figshare.com/s/fe1ab60f2a3ebcaae7ff

Single-cell RNA Seq Data

Patras (SYNGAP1p.Q503X) matrix.mtx.gz https://figshare.com/s/1cd0dc51bcf6f1028cd2

Patras (SYNGAP1p.Q503X) features.tsv.gz https://figshare.com/s/c08cfabef967271dcfbb

Patras (SYNGAP1p.Q503X) barcodes.tsv.gz https://figshare.com/s/2b493cc0108d5f2cbc35

D2 (Corrected) matrix.mtx.gz https://figshare.com/s/5b8b4b0cd4818c9c2e7d

D2 (Corrected) features.tsv.gz https://figshare.com/s/d6054204bd0514a87b5e

D2 (Corrected) barcodes.tsv.gz https://figshare.com/s/c1684604c58b0b04ba05

Proteomics PRIDE : PXD029230 (Username: reviewer_pxd029230@ebi.ac.uk

Password: grLXyKRz)

Figure 1

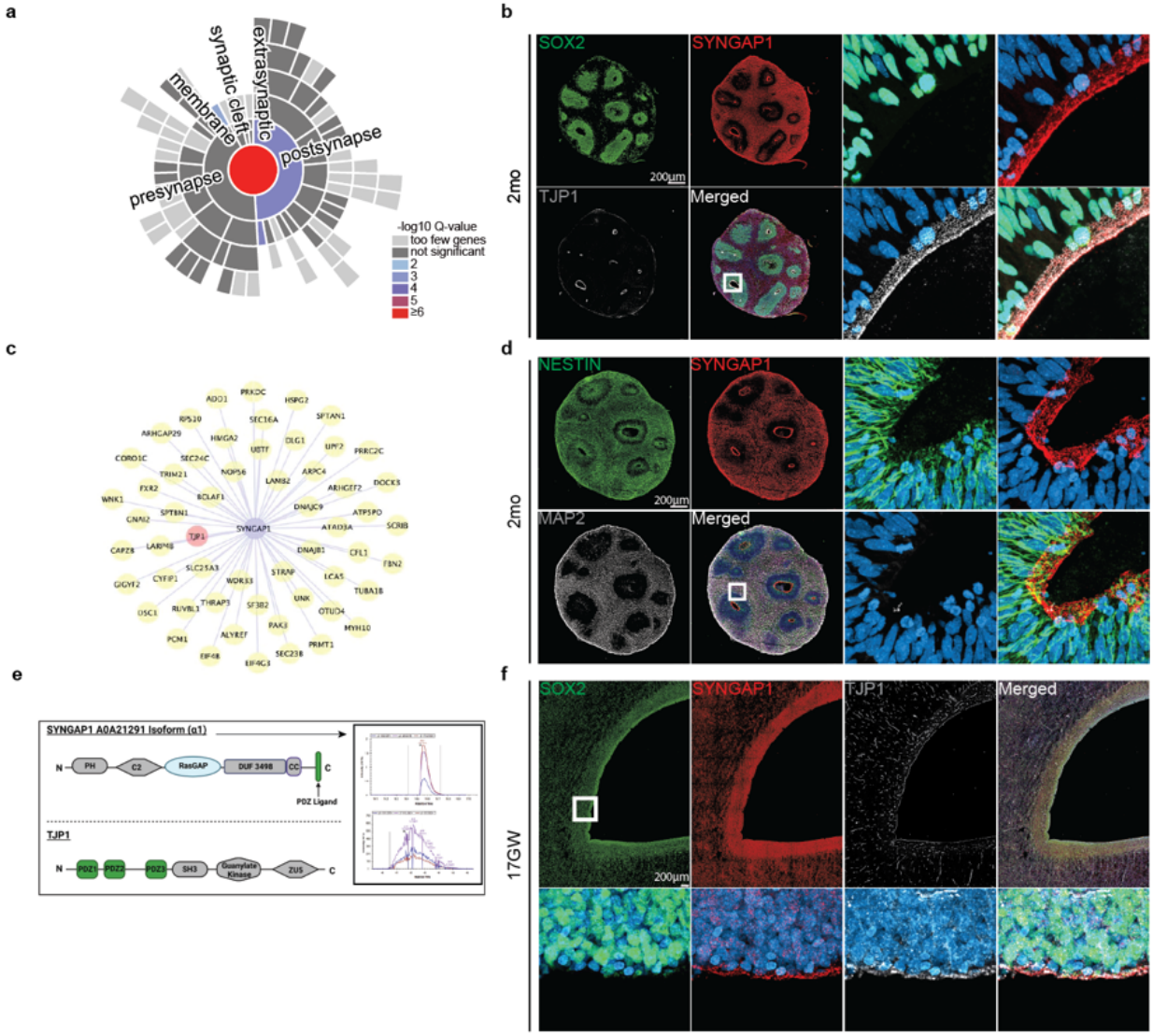

Figure 1. SYNGAP1 is expressed in human radial glia progenitors and colocalizes with the tight junction protein TJP1.

A. SynGO analysis results from D.I.V. 7 corrected organoids proteomic data set.

B. Two-month-old control organoid stained for the neural progenitor marker Sox2, the tight junction protein TJP1 and SYNGAP1. SYNGAP1 is highly expressed at the ventricular wall. White box indicates the region of interest selected for the merged images showing colocalization of the nuclear marker DAPI, TJP1, and SYNGAP1.

C. Schematic for the protein interaction network of SYNGAP1. The adherens junction protein TJP1 is highlighted in pink.

D. Two-month-old control organoid stained for the radial glial marker Nestin, the neuronal marker MAP2, and SYNGAP1. SYNGAP1 is highly expressed within mature MAP2 positive neuronal populations outside of the VZ, as well as in Nestin positive cells at the ventricle wall. White box indicates the region of interest selected for the merged images showing colocalization of DAPI, SYNGAP1, and Nestin positive cells.

E. Schematic of key functional domains within the SYNGAP1 alpha 1 isoform and TJP1 proteins including representative spectra of the two identified peptides for the SYNGAP1 alpha1 isoform.

F. Immunohistochemical staining of the human brain at gestational week 17. Tissue section is from the prefrontal cortex at the level of the lateral ventricle and medial ganglionic eminence. White box indicates the region of interest selected for the merged images showing colocalization of DAPI, TJP1, and SYNGAP1.

Figure 2

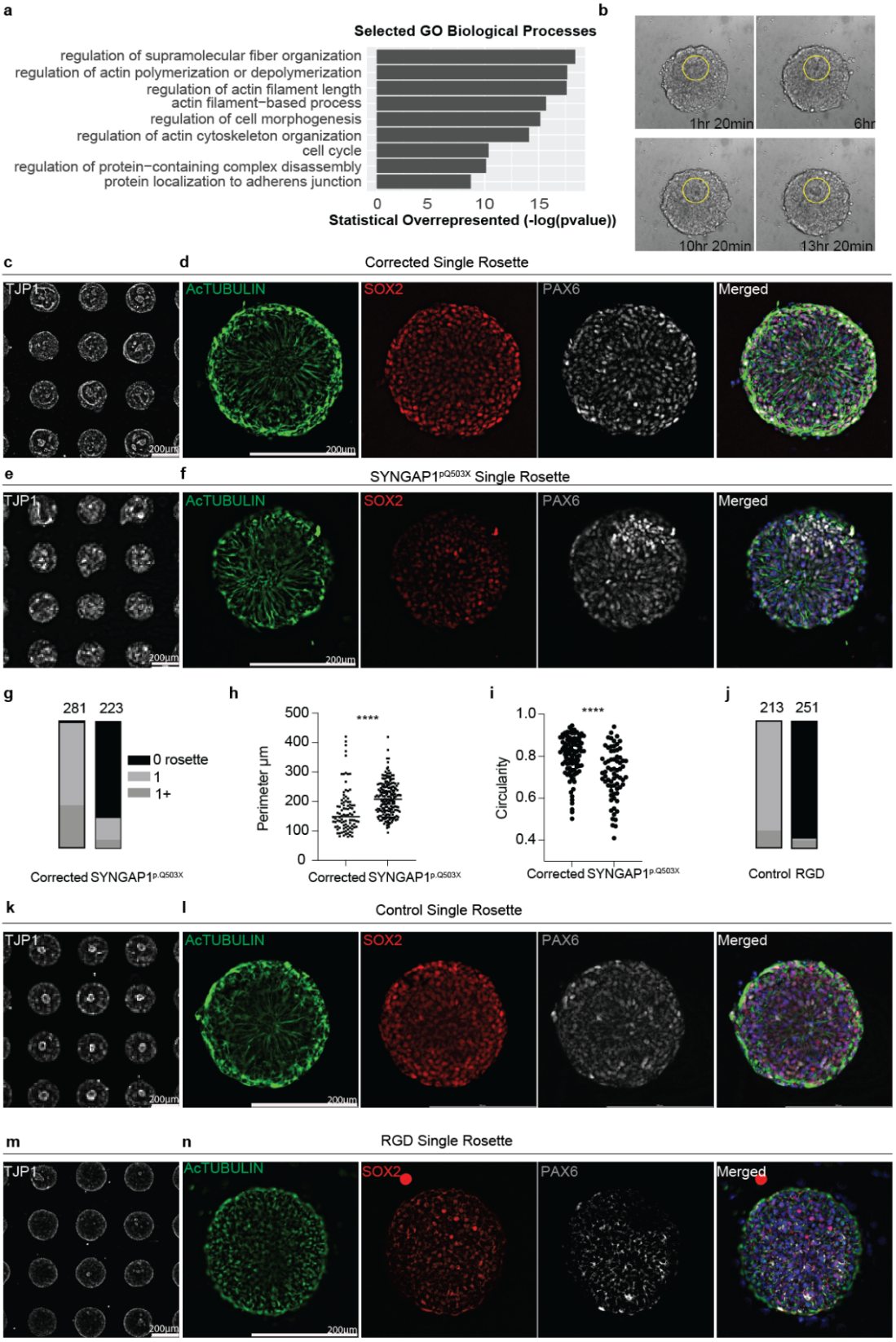

Figure 2. SYNGAP1 RASGAP domain is needed for cytoskeletal organization in human radial glia.

A. Selected GO terms for biological processes for bulk RNA sequencing data collected from D.I.V. 7 control organoids.

B. Still frames taken from live imaging of corrected rosette formation from day 5 to day 7 after initial seeding.

C. Array of single rosettes generated from the corrected line control labeled with TJP1 staining.

D. A single rosette generated from corrected iPSCs. The rosette is composed of cells positive for the neural stem cell marker Sox2 and radial glial progenitors positive for Pax6. Acetylated tubulin labels the microtubules of radial glial progenitors and highlights their radial organization around the luminal space.

E. Array of single rosettes generated from the SYNGAP1$^{p.Q503X}$ line labeled with TJP1 staining.

F. A single rosette generated from SYNGAP1$^{p.Q503X}$ iPSCs. Similar to the corrected rosette, it is composed of cells positive for Sox2 and Pax6. Acetylated tubulin labels the microtubules of radial glial progenitors and shows diminished radial organization around the luminal space as compared to the corrected rosette.

G. Quantification of the number of rosettes successfully formed in the corrected and SYNGAP1$^{p.Q503X}$ lines. Successful rosette formation was defined as containing a densely packed central area positive for TJP1 and radial organization of surrounding progenitor cells. N=281 control single rosettes and n= 223 SYNGAP1$^{p.Q503X}$ single rosettes from 3 independent experiments.

H. Quantification of the rosette lumen perimeter, as marked by TJP1 labeling in the corrected and SYNGAP1$^{p.Q503X}$ lines. Unpaired t-test was performed on n=94 corrected single rosettes and n= 198 SYNGAP1$^{p.Q503X}$ single rosettes from 3 independent experiments. P value <0.0001.

I. Quantification of the circularity of the rosette lumen as marked by TJP1 labeling in the corrected and SYNGAP1$^{p.Q503X}$ lines. Unpaired t-test was performed on n=99 corrected single rosettes and n= 69 SYNGAP1$^{p.Q503X}$ single rosettes from 3 independent experiments. P value <0.0001.

J. Quantification of the number of rosettes successfully formed in the control and RGD lines. Successful rosette formation was defined as containing a densely packed central area positive for TJP1 and radial organization of surrounding progenitor cells. N=213 control single rosettes and n= 251 SYNGAP1$^{p.Q503X}$ single rosettes.

K. Array of single rosettes generated from the control line labeled with TJP1 staining.

L. A single rosette generated from control iPSCs. The rosette is composed of cells positive for the neural stem cell marker Sox2 and radial glial progenitors positive for Pax6. Acetylated tubulin labels the microtubules of radial glial progenitors and highlights their radial organization around the luminal space.

M. Array of single rosettes generated from the RGD line labeled with TJP1 staining.

N. A single rosette generated from RGD iPSCs. Similar to the control rosette, it is composed of cells positive for Sox2 and Pax6. Acetylated tubulin labels the microtubules of radial glial progenitors and shows little to no radial organization or central luminal space.

Figure 3

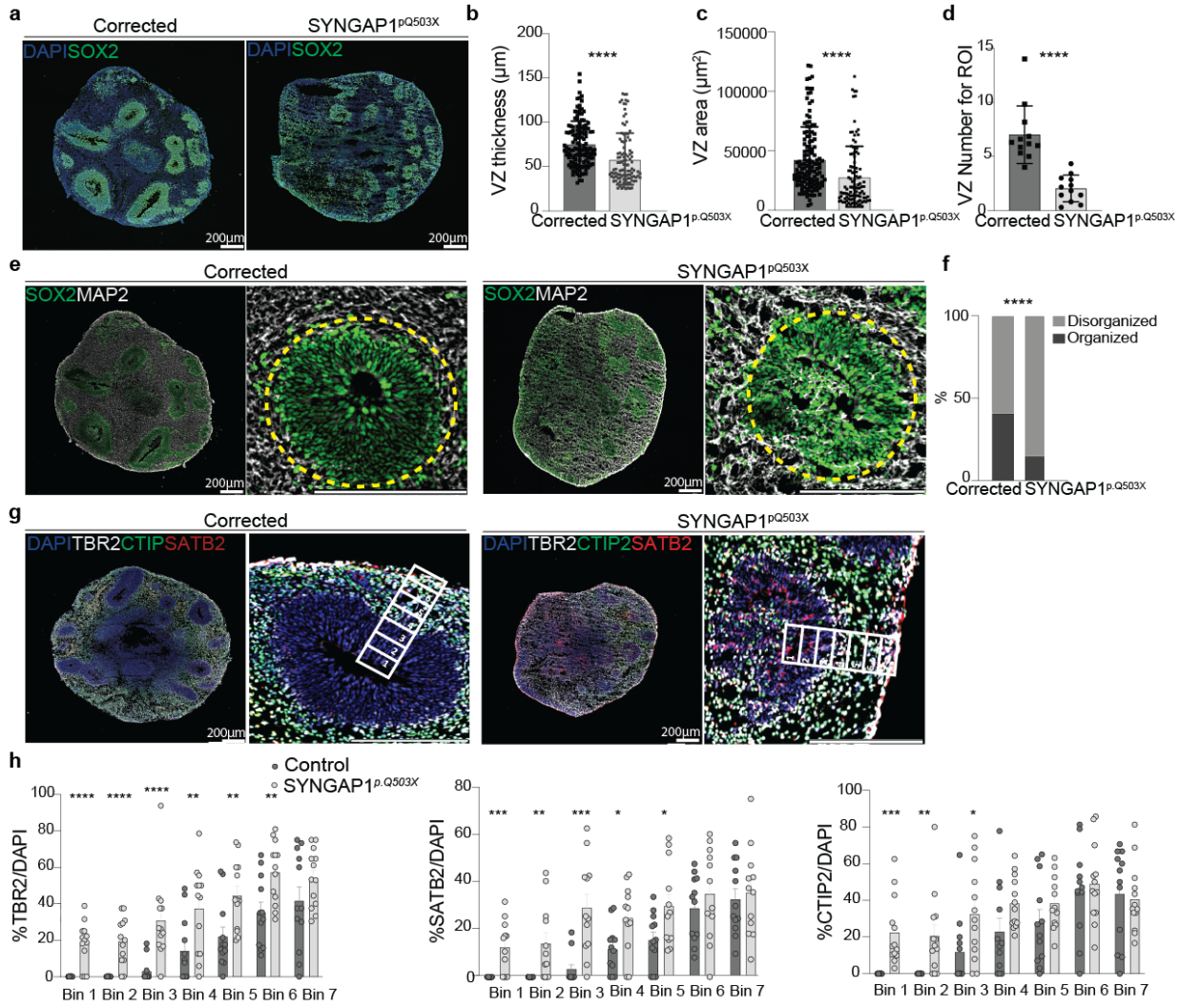

Figure 3. SYNGAP1 haploinsufficiency disrupts the organization of the developing cortical plate.

A. Two-month-old organoids show expression of Sox2, a neural stem cell marker, and nuclei marker DAPI. Corrected organoids display Sox2 expression exclusively within the ventricular zone (VZ), while SYNGAP1$^{p.Q503X}$ organoids lack a defined VZ.

B. VZ analysis shows VZ thickness (µm) in SYNGAP1$^{p.Q503X}$ and corrected organoids. SYNGAP1$^{p.Q503X}$ organoids present less proliferative VZ compared to corrected. Student's t-test was performed on 4 independent experiments where 20-30 VZs from 3 organoids were analyzed in each experiment. Single dots represent individual VZs. P value <0.0001.

C. VZ analysis shows VZ area (µm^2) in SYNGAP1$^{p.Q503X}$ and corrected organoids. SYNGAP1$^{p.Q503X}$ organoids present less extended VZ compared to corrected. Student's t-test was performed on 4 independent experiments where 20-30 VZs from 3 organoids were analyzed in each experiment. Single dots represent individual VZs. P value (<0.0001).

D. VZ analysis shows VZ number per Region of Interest (ROI) in SYNGAP1$^{p.Q503X}$ and corrected organoids. SYNGAP1$^{p.Q503X}$ organoids present fewer VZs compared to corrected. Mann Whitney test was performed on 4 independent experiments where 3-6 ROI from 3 organoids were analyzed in each experiment. Single dots represent the mean number of VZs per ROI in individual organoids. P value (<0.0001).

E. Two-month-old organoids show expression of Sox2 and microtubule associated protein-2 (MAP2), a pan-neuronal marker. Corrected organoids display Sox2 expression in the VZ, while MAP2 labels neurons that have migrated away from the VZ and now populate the cortical plate. SYNGAP1$^{p.Q503X}$ organoids display Sox2 expression in the VZ and MAP positive neurons inside and outside of the VZ, indicating impaired migration of neurons away from the VZ. Dashed yellow circles identify VZ regions.

F. Quantification of the occurrence of organized versus disorganized VZ structures in corrected and SYNGAP1$^{p.Q503X}$ organoids based on Sox2 and MAP2 staining patterns. Chi-square test was performed on mean values of VZ from 3-9 ROI of 3 organoids, analyzed in 4 independent experiments. P value <0.0001.

G. Corrected organoids stained for the neuronal markers CTIP2, SATB2, and the intermediate progenitor marker TBR2. Close up image shows pseudo layering stratification with SATB2

and CTIP2 positive cells expressed more abundantly in bins occupying areas outside of the VZ. SYNGAP1$^{p.Q503X}$ organoids stained for the neuronal markers CTIP2, SATB2, and the intermediate progenitor marker TBR2. Close up image shows a disruption of the pseudo layering stratification, highlighted by white numbered ladder.

H. Binning analysis for TBR2, SATB2, and CTIP2. Student's t-test was performed on a total 12 ventricles for each condition from 3 independent experiments. *P value = 0.01, ** P Value <0.01, *** P Value <0.001, **** P Value <0.0001.

Figure 4

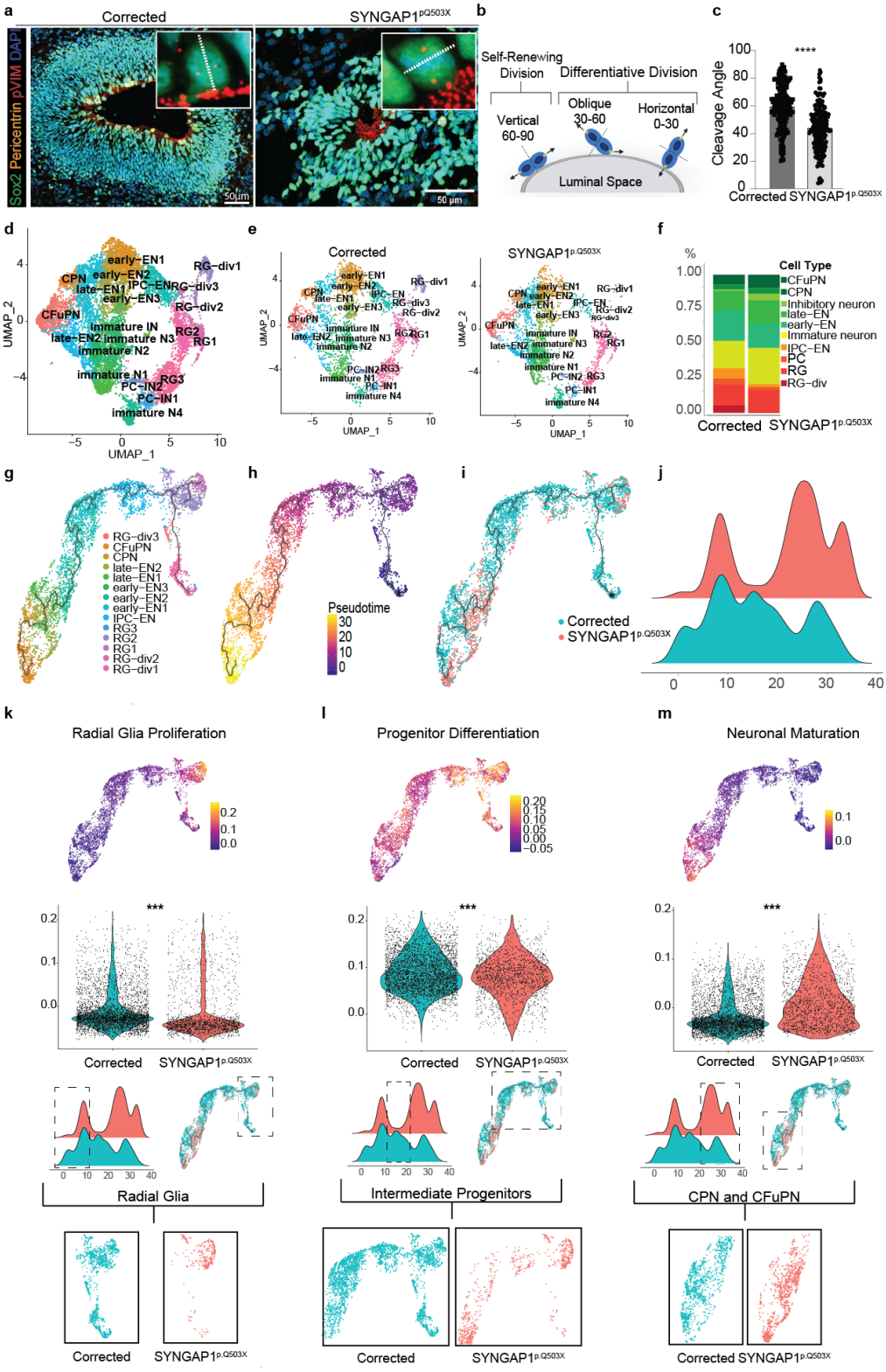

Figure 4. SYNGAP1 haploinsufficiency impairs the developmental trajectory of human radial Glial progenitors.

A. Control and SYNGAP1$^{p.Q503X}$ organoids display SOX2 expression in the VZ, dividing neural progenitors marked by phospho-vimentin (pVIM), and the centrosome labeling marker Pericentrin.

B. Schematic representation of cell divisions at the VZ wall. Schematic illustrates self-renewing divisions (vertical, with angle between 60 to 90 degrees from the apical wall to the mitotic spindle) and differentiative divisions (oblique, 30 to 60 degrees; horizontal, 0 to 30 degrees).

C. Cleavage angle analysis showing increased proliferative divisions in cells from control organoids and increased differentiative divisions from SYNGAP1$^{p.Q503X}$ organoids. Mann-Whitney test was performed on a total of 181 cells for condition, from 3 independent experiments. P.value < 0.0001

D. Combined t-distributed stochastic neighbor embedding (t-SNE) analysis of all organoids at 4 months.

E. (Left) t-distributed stochastic neighbor embedding (t-SNE) analysis of corrected organoids at 4 months. Total cell population was randomly downsampled. (Right) t-distributed stochastic neighbor embedding (t-SNE) analysis of Syngap haploinsufficient organoids at 4 months.

F. Percentage of cell types per cell line color coded by cell type.

G. Pseudotime UMAP for combined datasets color coded by cell type

H. Pseudotime UMAP for combined datasets (blue, early to yellow, late).

I. Pseudotime UMAP for individual datasets with SYNGAP1$^{p.Q503X}$ in red and corrected in blue.

J. Pseudotime distribution across individual datasets with SYNGAP1$^{p.Q503X}$ in red and corrected in blue.

K. Radial glial proliferation module of highly correlated genes. Upper panel: UMAP plot of module scores; lower panel: score distribution across the genotypes. P value=9.7226e-65.

Bottom panel: cells within partitions of interest identified to be associated with the corresponding module of highly correlated genes for radial glia proliferation.

L. Progenitor differentiation module of highly correlated genes. Upper panel: UMAP plot of module scores; lower panel: score distribution across the genotypes. P value= 3.458691e-08. Bottom panel: cells within partitions of interest identified to be associated with the corresponding module of highly correlated genes for progenitor differentiation.

M. Neuronal maturation module of highly correlated genes. Upper panel: UMAP plot of module scores; lower panel: score distribution across the genotypes. P value=1.051494e-101. Bottom panel: cells within partitions of interest identified to be associated with the corresponding module of highly correlated genes for neuronal maturation.

Figure 5

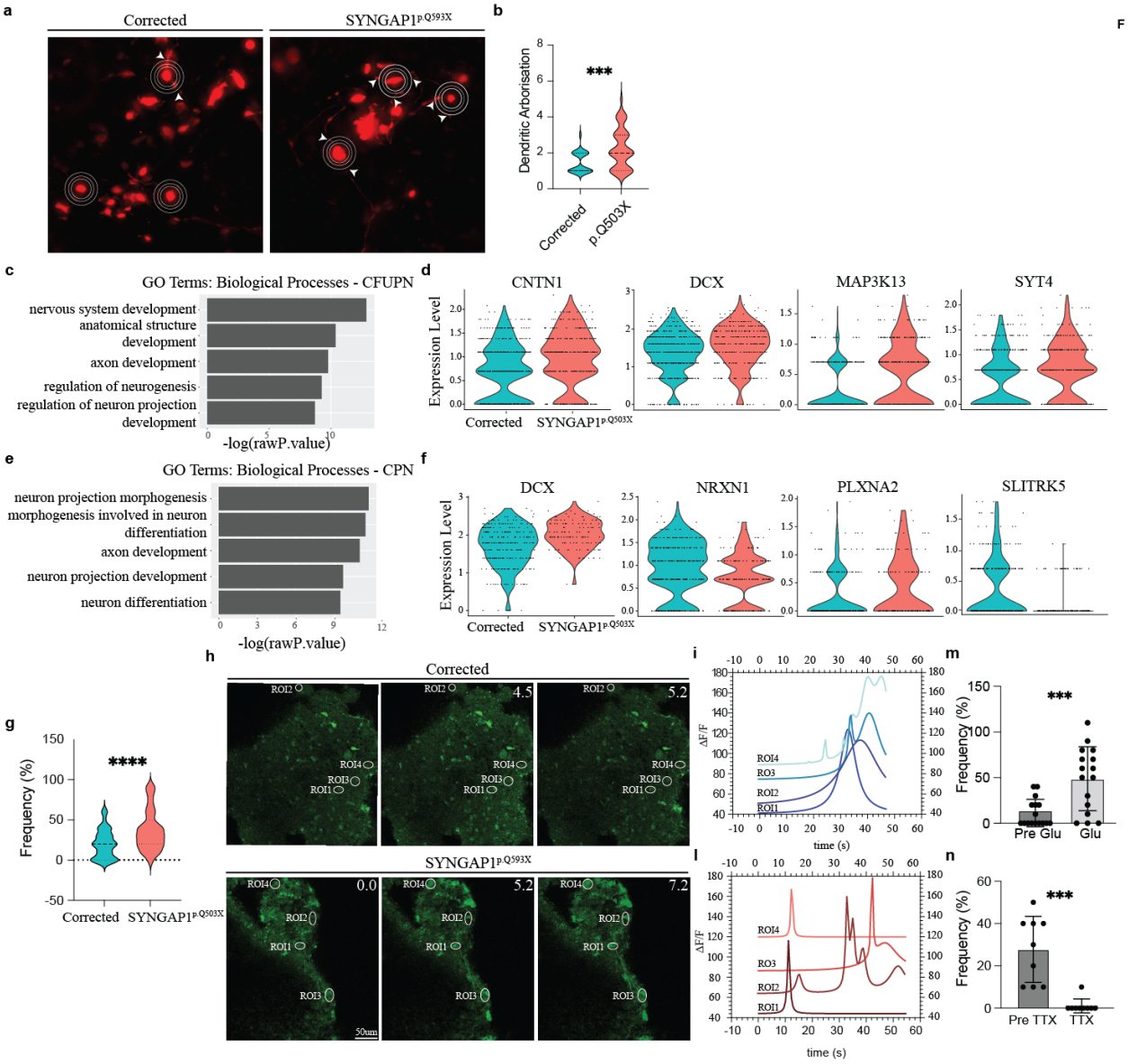

Figure 5. SYNGAP1 organoids exhibit accelerated maturation of cortical projection neurons.

A. Representative images of RFP positive neurons from 4-month-old organoids used for dendritic arborization analysis.

B. Dendritic arborisation analysis on 4-month-old corrected and SYNGAP1$^{p.Q503X}$ organoids. Unpaired t-test performed on a total of 28 cells for corrected organoids and 49 cells for SYNGAP1$^{p.Q503X}$ organoids, from 3 independent experiments. P value= 0.0009.

C. Selected GO Terms for biological processes of 4-month-old organoid single cell dataset for CFuPN.

D. Violin plot for selected genes showing expression levels between corrected and SYNGAP1$^{p.Q503X}$ organoids. DCX (Adj. P value = 0.04153089), CNTN1 (Adj. P value = 4.39E-07), SYT4 (Adj. P value = 6.77E-06)

E. Selected GO terms for biological processes of 4-month-old organoid single cell dataset for CPN.

F. Violin plot for selected genes showing expression levels between corrected and SYNGAP1$^{p.Q503X}$ organoids. DCX (Adj. P value = 0.00040542), PLXNA2 (P value =0.00031511), SLYTRK5 (P value = 3E-06)

G. Calcium spike frequency analysis on 2-month-old corrected and SYNGAP1$^{p.Q503X}$ organoids. Unpaired t-test performed on a total of 54 cells for corrected organoids and 54 cells for SYNGAP1$^{p.Q503X}$ organoids, from 3 independent experiments. P value <0.0001.

H. Frames at different time points (mins) of video recordings from GCaMP6f2 corrected and SYNGAP1$^{p.Q503X}$ organoids. Yellow circles highlight Regions of Interest (ROI). Right Panel: each ROI is plotted for average intensity over time.

I. ΔF/F(t) of selected ROIs from GCaMP6f2 recordings of corrected organoids.

J. ΔF/F(t) of selected ROIs from GCaMP6f2 recordings of SYNGAP1$^{p.Q503X}$ organoids.

K. Calcium spike frequency analysis on 2-month-old SYNGAP1$^{p.Q503X}$ organoids before and during bath application of glutamate (Glu). Unpaired t-test performed on a total of 16 cells from SYNGAP1$^{p.Q503X}$ organoids, from 3 independent experiments. P value = 0.0005.

L. Calcium spike frequency analysis on 2-month-old SYNGAP1$^{p.Q503X}$ organoids before and during bath application of tetrodotoxin (TTX). Unpaired t-test performed on a total of 9 cells from SYNGAP1$^{p.Q503X}$ organoids, from 3 independent experiments. P value =0.0001.

Supplementary Figure 1

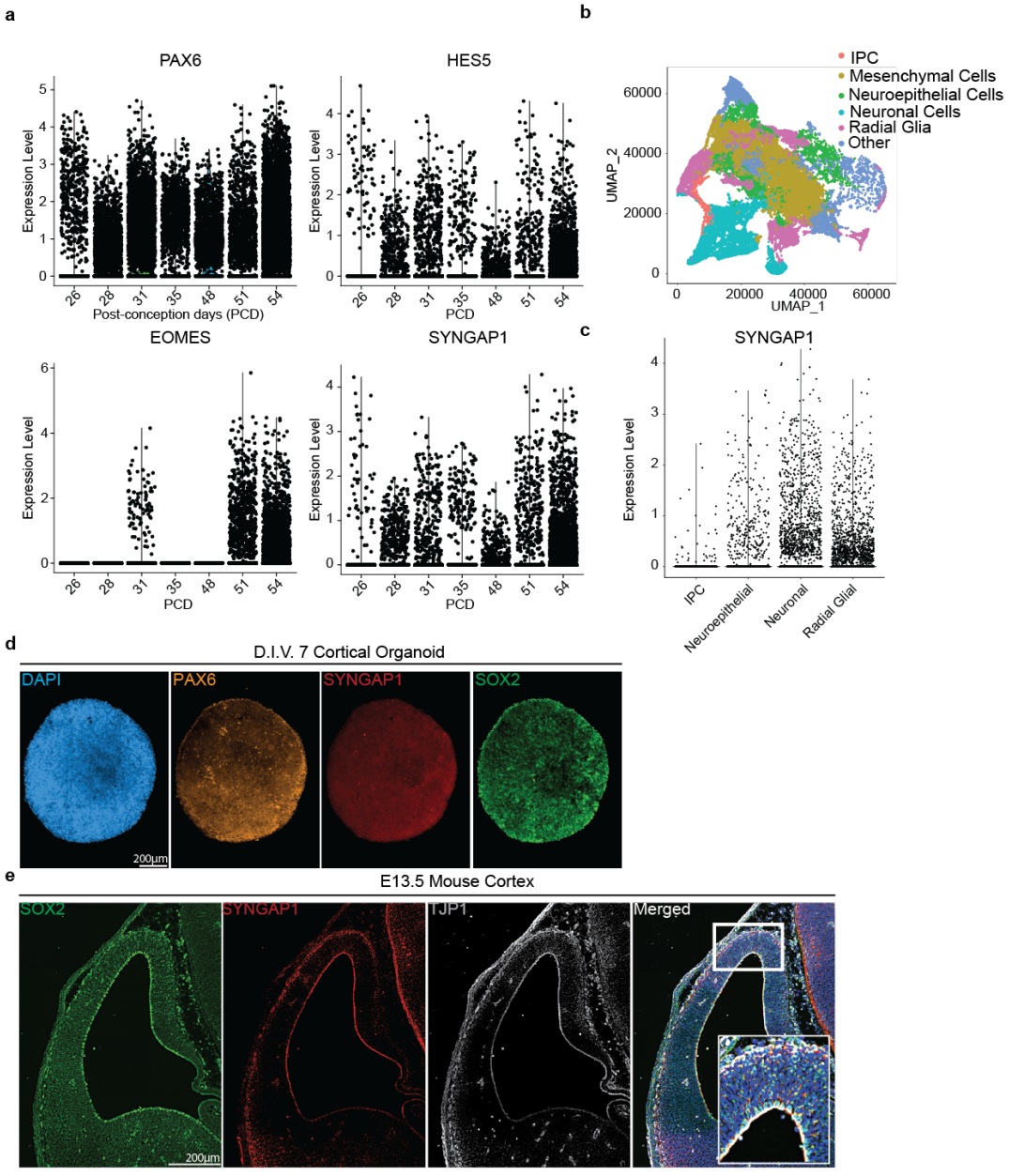

Supplementary Figure 1

A. Expression of early forebrain marker genes of PAX6, HES5, EOMES (TBR2) and SYNGAP1 from post-conception day (PCD) 26 to 54 from single cell RNA-seq data.
B. UMAP visualization of age-dependent clustering of fetal single cells.
C. SYNGAP1 expression at PCD 56 grouped by cell types; intermediate progenitor cells (IPC), neuroepithelial cells (NE), radial glial cells (RGCs) and neurons.
D. D.I.V. 7 cortical organoids are composed of cells positive for the neural stem cell marker SOX2, the radial glial progenitor marker PAX6, and SYNGAP1.
E. A coronal section from E13.5 mouse brain showing expression of the neural stem cell marker SOX2, the tight junction protein TJP1, and SYNGAP1. SYNGAP1 is highly expressed at the ventricular wall. White box indicates the Region of Interest selected for the merged images showing colocalization of DAPI, TJP1, and SYNGAP1.

Supplementary Figure 2

a

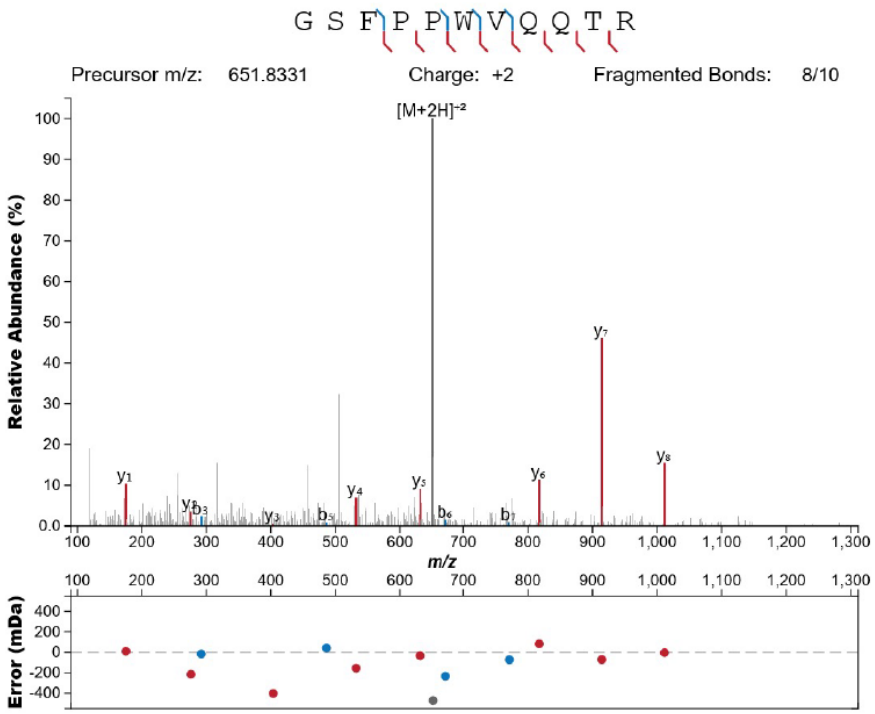

b

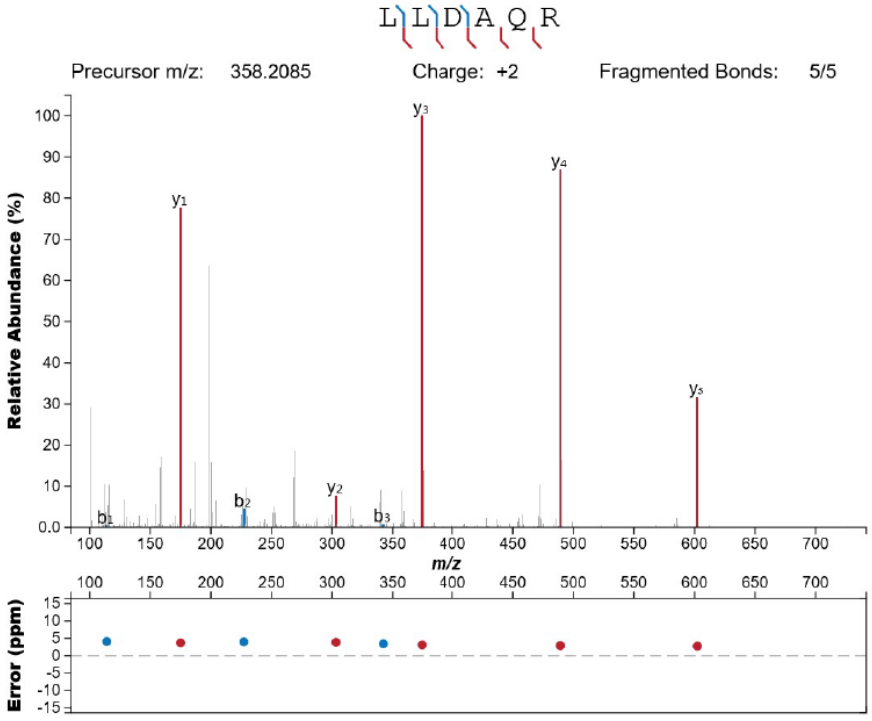

Supplementary Figure 2

A. Annotated spectra of the SYNGAP1 isoform alpha 1 specific peptide "GSFPPWQQTR" identified from MS analysis of immune-isolated SYNGAP1 protein from D.I.V. 7 organoids.

B. Annotated spectra of the SYNGAP1 isoform alpha 1 specific peptide "LLDAQR" identified from MS analysis of immune-isolated SYNGAP1 protein from D.I.V. 7 organoids.

Supplementary Figure 3

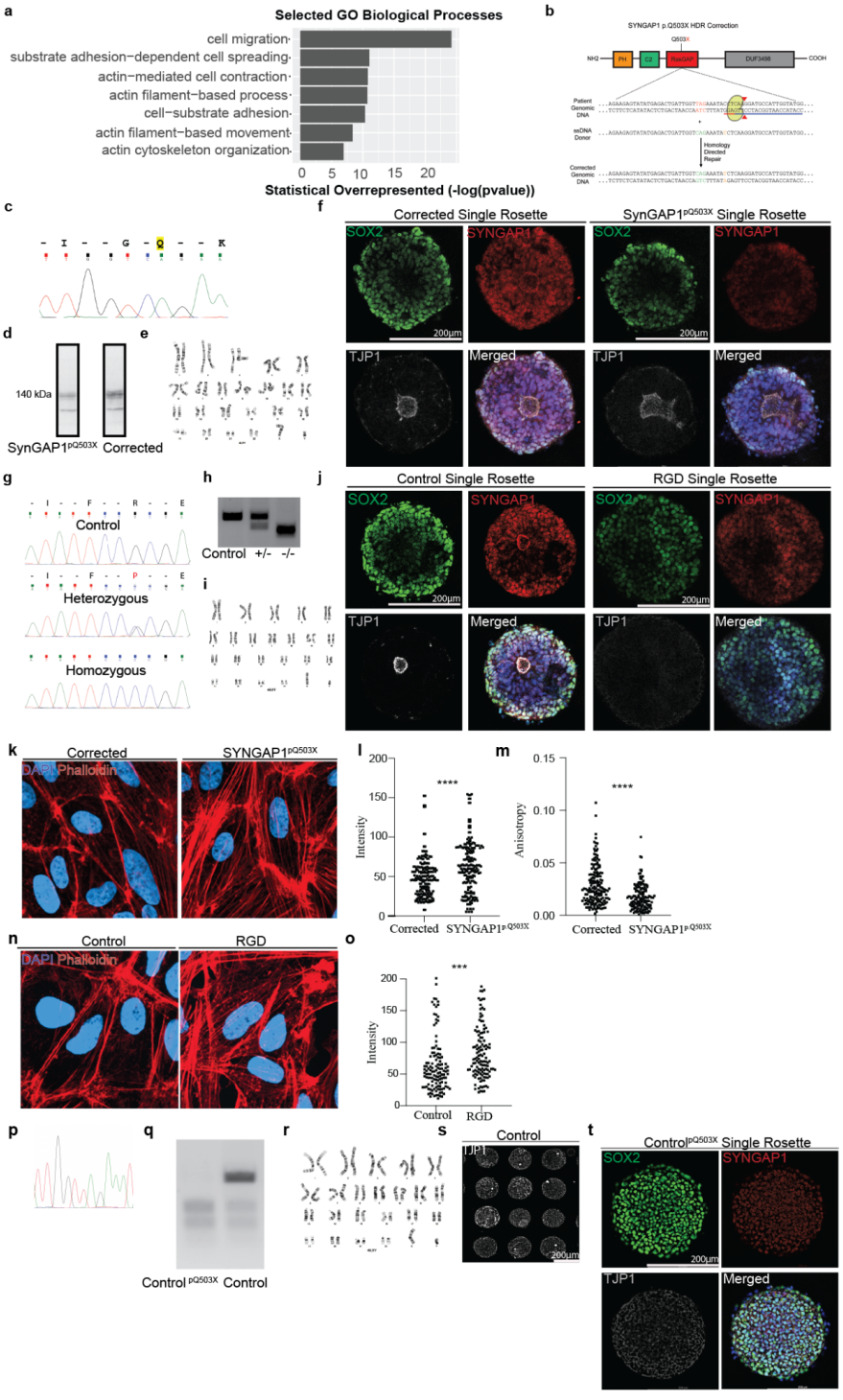

Supplementary Figure 3

A. Selected GO terms for biological processes for SYNGAP1 immunoprecipitation data collected from D.I.V. 7 cortical organoids.
B. Schematic of line generation details for isogenic control of SYNGAP1$^{p.Q503X}$.
C. Chromatogram of the generated corrected line.
D. Western blot for SYNGAP1 in SYNGAP1$^{p.Q503X}$ and corrected line.
E. Corrected line with normal karyotype.
F. A single rosette generated from corrected and SYNGAP1$^{p.Q503X}$ iPSCs. Both rosettes are composed of cells positive for the neural progenitor marker Sox2 and SYNGAP1. SYNGAP1 is also highly expressed at the apical wall of the lumen. The tight junction protein TJP1 labels the central luminal space of the rosette. Merged images show colocalization of DAPI, SYNGAP1, and TJP1. The TJP1 positive area is often larger and more irregularly shaped as compared to controls.
G. Chromatogram of the RasGap Dead-line (RGD) (-/-), Control (+/+) and Heterozygous lines (+/-).
H. Western blot for SYNGAP1 in RGD(-/-), Control (+/+) and Heterozygous lines (+/-).
I. RGD line with normal karyotype.
J. A single rosette generated from control and RGD iPSCs. Both rosettes are composed of cells positive for the neural progenitor marker Sox2 and SYNGAP1. In control rosettes, SYNGAP1 is also highly expressed at the apical wall of the lumen and the tight junction protein TJP1 labels the central luminal space of the rosette. Merged image shows colocalization of DAPI, SYNGAP1, and TJP1. However, in the RGD rosette there is no defined central luminal space and therefore no specific TJP1 labeling.
K. 2D human radial glial progenitor cells after being dissociated from corrected and SYNGAP1$^{p.Q503X}$ D.I.V. 7 organoids. Cells are stained with phalloidin to label actin filaments and DAPI to label nuclei.
L. Quantification of fluorescent intensity of the phalloidin staining. SYNGAP1p.Q503X cells exhibit higher levels of fluorescent intensity for phalloidin staining, indicating a greater abundance of actin filaments. Unpaired t-test was performed on a total of 211 cells for each condition from 3 independent experiments. P value <0.0001.

M. Quantification of the anisotropy, or organization, of the actin filaments. SYNGAP1p.Q503X cells display lower levels of anisotropy, indicating decreased organization of the actin filaments. Unpaired t-test was performed on a total of 202 cells for each condition from 3 independent experiments. P value <0.0001.

N. 2D human radial glial progenitor cells after being dissociated from control and RGD D.I.V. 7 organoids. Cells are stained with phalloidin to label actin filaments and DAPI to label nuclei.

O. Quantification of fluorescent intensity of the phalloidin staining. RGD cells exhibit higher levels of fluorescent intensity for phalloidin staining indicating a greater abundance of actin filaments. Unpaired t-test was performed on a total of 125 cells for each condition from 3 independent experiments. P value <0.0002.

P. Chromatogram of the Control p.Q503X line.

Q. Western blot for SYNGAP1 in Control p.Q503X and Control line.

R. Control p.Q503X line with normal karyotype.

S. Array of single rosettes generated from the SYNGAP1p.Q503X line and labeled with TJP1 staining.

T. A single rosette generated from Control p.Q503X iPSCs. The rosette is composed of cells positive for the neural progenitor marker Sox2 and SYNGAP1. SYNGAP1 is highly expressed at the apical wall of the lumen, and the tight junction protein TJP1 labels the central luminal space of the rosette. Merged image shows colocalization of DAPI, SYNGAP1, and TJP1.

Supplementary Figure 4

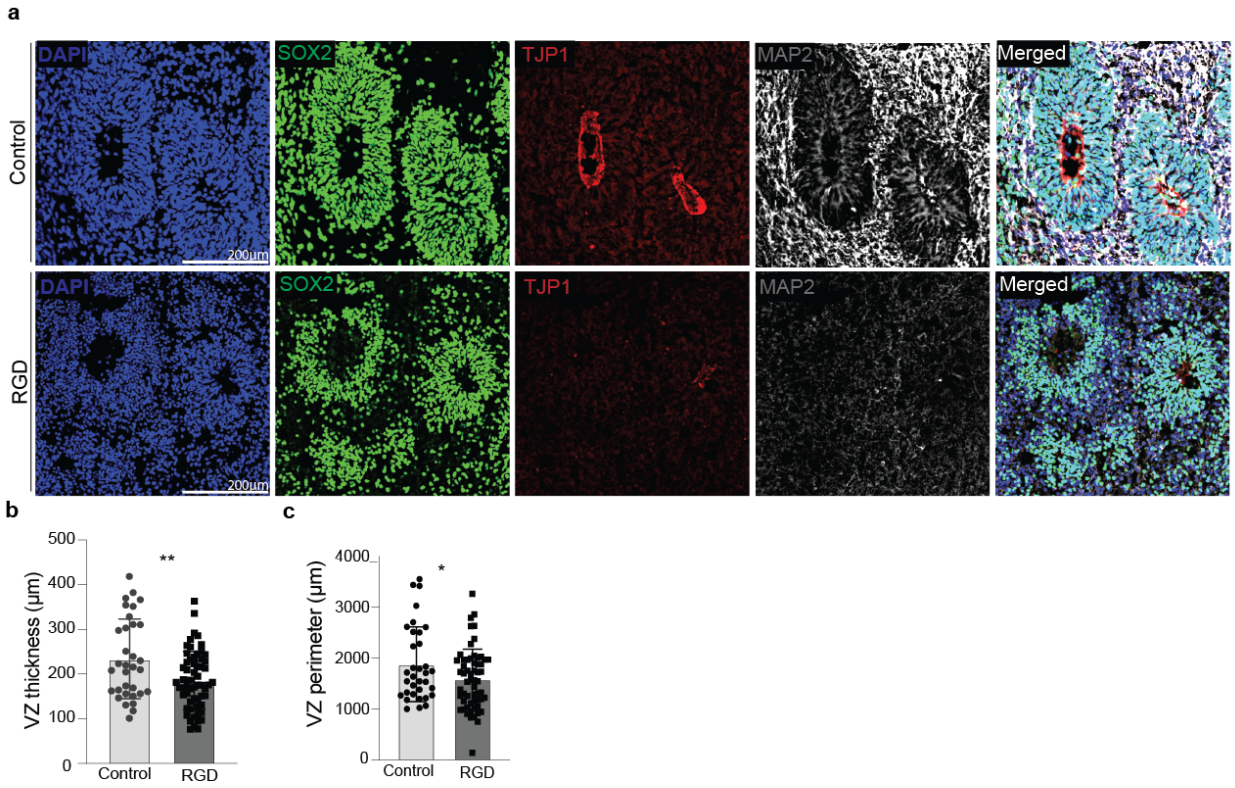

Supplementary Figure 4

A. Select regions of 2-month-old control and RGD organoids highlighting the organization of their respective ventricular zones. RGD organoids have little to no specific TJP1 expression and disorganized MAP2 expression as compared to control.
B. Quantification of ventricular zone (VZ) thickness as defined by Sox2 labeling. VZ thickness is reduced in RGD organoids. Student's t-test was performed on 3 independent experiments where 33 control and 59 RGD VZs from 3 organoids were analyzed in total. Single dots represent individual VZs. P value =0.0037.
C. Quantification of VZ perimeter as defined by Sox2 labeling. VZ is reduced in RGD organoids. Student's t-test was performed on 3 independent experiments where 33 control and 59 RGD VZs from 3 organoids were analyzed in total. Single dots represent individual VZs. P value =0.0385.

Supplementary Figure 5

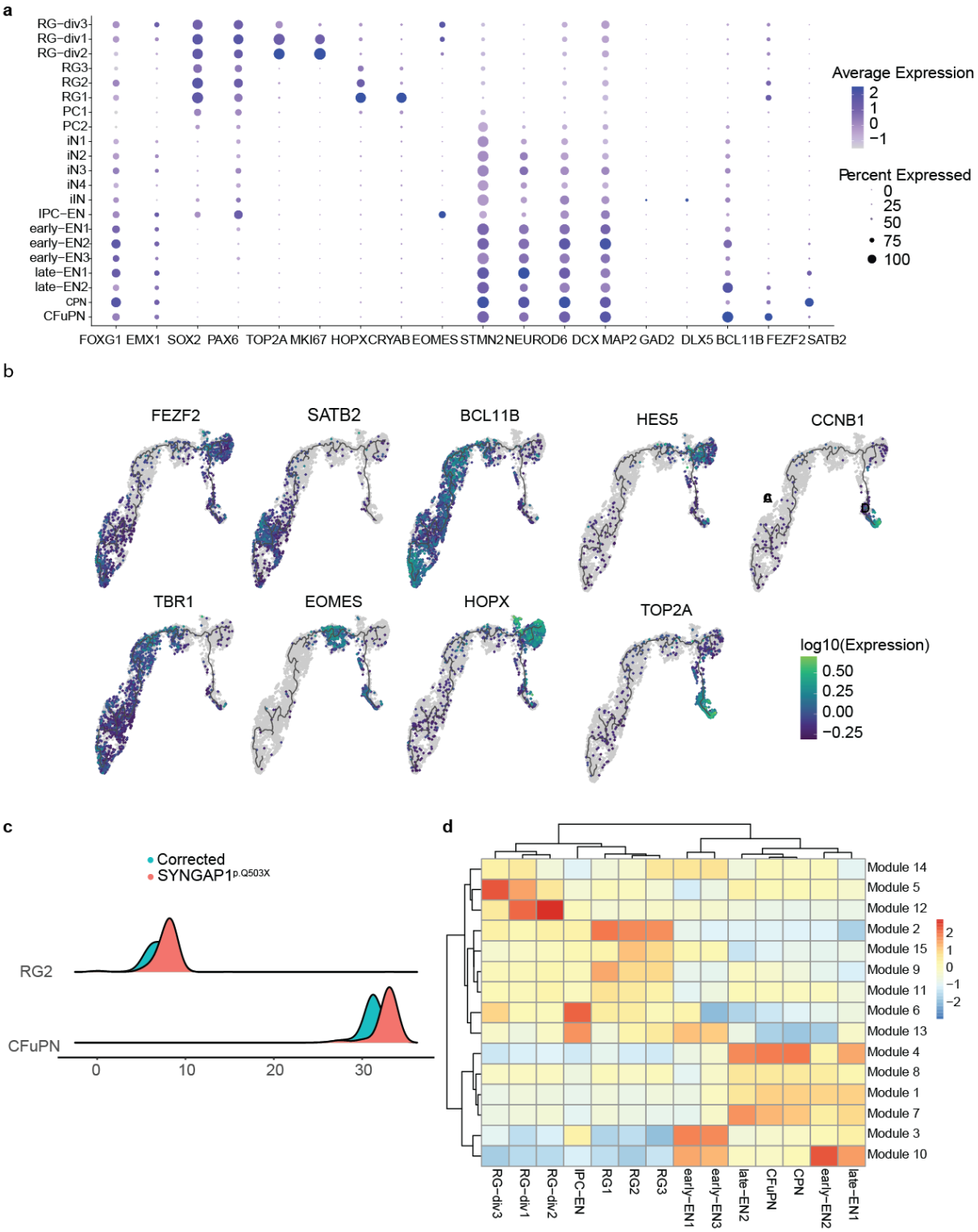

Supplementary Figure 5

A. Dot plot showing marker genes used to classify cell clusters identified from single cell sequencing of 3-month-old corrected and SYNGAP1$^{p.Q503X}$ organoids. Size of the dot is indicative of the percent of cells expressing the gene, color of the dot is indicative of the average expression level.
B. Pseudotime distribution across individual datasets in RG2 and CFuPN cells with SYNGAP1$^{p.Q503X}$ in red and corrected in blue.
C. Pseudotime UMAP with log expression of selected genes. Genes for cycling cells (TOP2A, HES5, CCNB1), radial glial progenitors (FEZF2, HOPX, EOMES), and neurons (TBR1, SATB2 and BCL11B) are highlighted.
D. Heatmap for all gene modules across cell types.

Supplementary Table 1

Proteome of 7 D.I.V. Cortical Organoids.

Supplementary Table 2

SynGO analysis of 7 D.I.V. Cortical Organoids Proteome.

Supplementary Table 3

Interactome of SYNGAP1 in 7 D.I.V. Cortical Organoids.

Supplementary Table 4

Differential Expression Analysis (DEGs) from Bulk-RNA sequencing of 7 D.I.V. Cortical Organoids from SYNGAP1$^{p.Q503X}$ and corrected line.

Supplementary Table 5

Differential Expression Analysis (DEGs) from sc-RNA sequencing of 4 month-old Cortical Organoids from SYNGAP1$^{p.Q503X}$ and corrected line.

Supplementary Video 1

Live imaging of corrected rosette formation from day 5 to day 7 after initial seeding.

Supplementary Video 2

Live imaging of SYNGAP1$^{p.Q503X}$ rosette formation from day 5 to day 7 after initial seeding.

Supplementary Video 3

10 minutes video recordings of GCaMP6f corrected organoids.

Supplementary Video 4

10 minutes video recordings of GCaMP6f SYNGAP1$^{p.Q503X}$ organoids.